SEISMIC EXPLORATION OF URANIUM DEPOSITS IN THE ATHABASCA BASIN, SASKATCHEWAN—A MODELLING STUDY

by

Dong Shi

A research report submitted in conformity with the requirements
for the degree of Master of Science
Graduate Department of Earth Sciences
University of Toronto

Acknowledgements

Contents

List of Tables

List of Figures

Chapter 1

Introduction

The Athabasca Basin, located in northern Saskatchewan and Alberta, holds the world's largest high-grade uranium deposit. A comprehensive study of Athabasca uranium deposit can be found in the Geological Survey of Canada EXTECH IV Bulletin (Jefferson et. al., 2007), which is associated with multidisciplinary research in the basin. Starting from 2013, the Canada Mining Innovation Council (CMIC), a collaborative research and development program of the Natural Sciences and Engineering Research Council of Canada (NSERC), initiated the Footprints project focusing on exploration of ore systems by integrated geological, geophysical and geochemical methods. The uranium exploration in the Athabasca Basin is planned to be one of the three Footprint research sites. Figure 1.1 shows the regional geology map of the Athabasca Basin. The uranium deposit is controlled by the unconformity between the Mesoproterozoic Athabasca sedimentary sequence and the Paleoproterozoic metamorphic basement rocks, and more than 90% of the known reserve is found in the eastern margin, where the P2 thrust fault holds the largest portion of the uranium deposit.

Seismic methods have been practised and proved to be useful tools for uranium exploration in the Athabasca Basin. White et. al. (2007) summarized previous petrophysical and seismic study in the McArthur River area that possesses major uranium production mines along the P2 thrust fault. Two high resolution surface seismic lines near the McArthur River mine were conducted (Figure 1.2), focusing on the detailed mapping of the basement unconformity (Györfi et. al., 2007). Other than the surface seismic lines, local petrophysical information was determined by the borehole geophysical logging (Mwenifumbo et. al., 2007) and the three-component (3C) vertical seismic profiling (VSP) surveys. After the exploration work in the McArthur River area, seismic survey has been moved on to the Millennium area located to the southwest of the McArthur River along the P2 fault (Juhojuntti et. al., 2012). The three-dimensional (3D) survey has been conducted and recorded by three-component geophones. Besides the mapping of basement unconformity, the 3D 3C survey is trying to image the orebody.

A petrophysical and reflectivity analysis of the subsurface near McArthur uranium deposits can be found in White et. al. (2007). Figure 1.3 shows the schematic sketch of the subsurface geology near the uranium mineralization. The reflectivity within the Athabasca group sandstone is estimated to be weak (R<0.05) and controlled mostly by porosity. The reflectivity of the unconformity, in contrast, is generally very strong (R=0.27-0.31) and intensely affected by the silicification alteration condition of the sandstone. The orebody, with small size compared to the seismic wavelet, is more likely to diffract the seismic wave rather than reflect it.
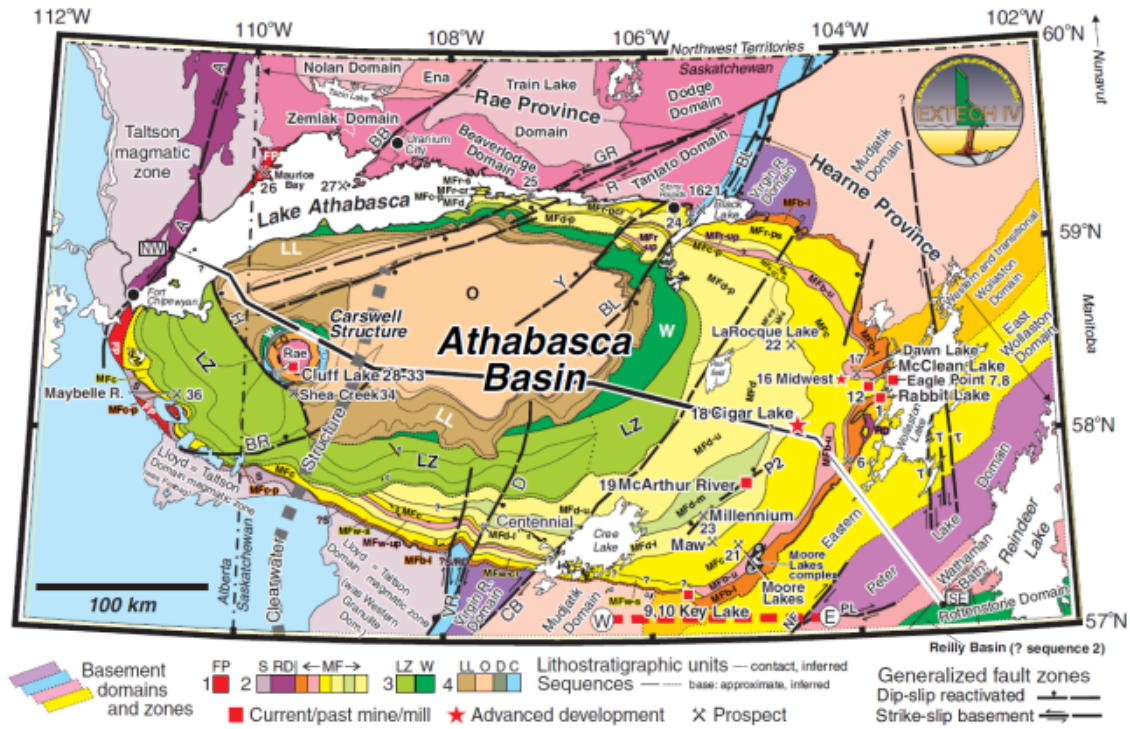
Figure 4. a) (See page 559 for caption).

Figure 1.1: Geological setting with unconformity-associated uranium occurrences of the Athabasca Basin region in northern Saskatchewan and Alberta by Jefferson et. al. (2007).
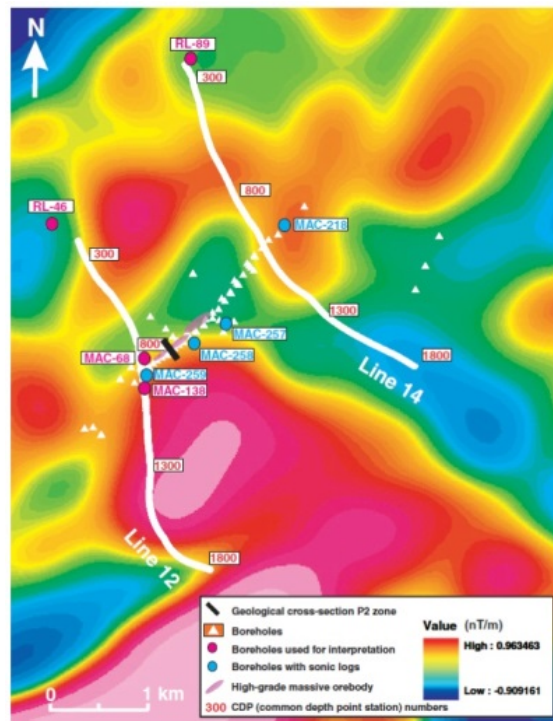
Figure 1.2: A location map of McArthur River high-resolution seismic lines and major borehole locations used in the seismic interpretation work by Gyorfi et. al. (2007).
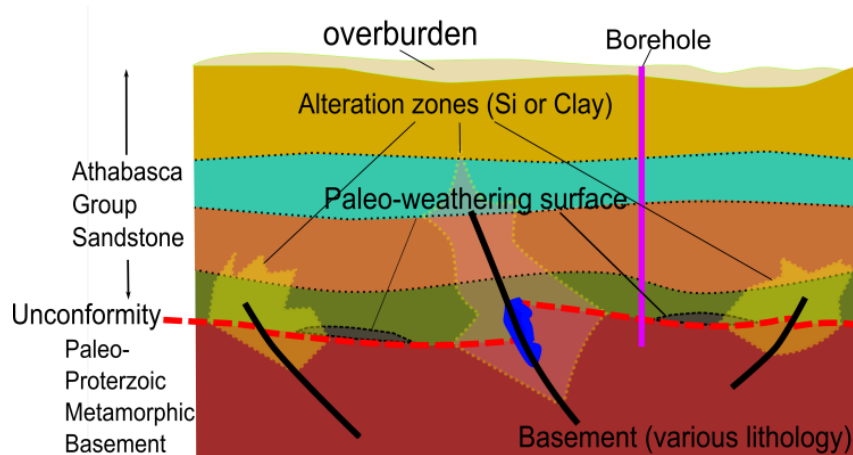
Figure 1.3: A schematic sketch of subsurface geology near uranium deposits (modified from Jefferson et al., 2007). The Athabasca Group sandstone is subdivided into four sandstone sequences.

Figure 1.4a shows a section of CDP stacked profile from high resolution seismic line 14 near the McArthur River mine. The dashed line and two question marks indicate where the interpretation of the basement unconformity becomes significantly difficult. Figure 1.4b shows the seismic section of the 3D 3C survey at Millennium near the uranium deposit. Loss of unconformity images can be found within the interpreted positions of alteration zone surrounding the uranium mineralization. The p-wave image loss on both 2D and 3D sections near the P2 mineralization zone is a major difficulty in the seismic interpretation.

The seismic data quality is controlled by either the variable p-wave reflectivity or the strong attenuation conditions for the uranium exploration in the Athabasca Basin. The mineralization of uranium deposits has been recognized to be associated with multiple stages of either silicification or argillization alterations (Hoeve and Sibbald, 1978), which accounts for a variable clay content in the sandstone. Hecht and Cuney (2000) also denoted that the ore bearing envelope can be observed in the basement rocks. The diverse alteration conditions lead to highly variable seismic velocities above and below the unconformity, resulting in an inconsistent reflectivity especially near a uranium ore body. Overburden controls the local seismic data attenuation conditions. Figure 1.5 shows an example of common-shot gather from one of the seismic high resolution line at McArthur River. The p-wave reflection (the hyperbola) is intensely smeared by the near surface events (ground roll and reverberation). Moreover, the direct arrived p-wave first break is strongly attenuated within the 200 m offset range, which implies a significant energy absorption along the surface overburden. Unconsolidated Quaternary glacial deposits, composed of poorly sorted sand and gravel, form the overburden with variable thickness (Schreiner, 1983). The underlying Athabasca group is mainly composed of highly fractured and brine saturated sandstone (Sun et. al., 2014). Intensely paleoweathered zones are observed overlying the surface of the basement unconformity. The attenuation mechanism with low confining pressure and highly mobilized fluids causes a significant energy loss during seismic wave propagation.

The project focuses on the investigation of the p-wave image loss of the basement unconformity based on numerical methods. The rock physical properties are obtained from in-situ borehole and VSP measurements. When primary reflected p-wave fails to create images of the unconformity, converted s-wave recorded in the 3D 3C Millennium survey, could be a useful tool for seismic exploration. The resolu-
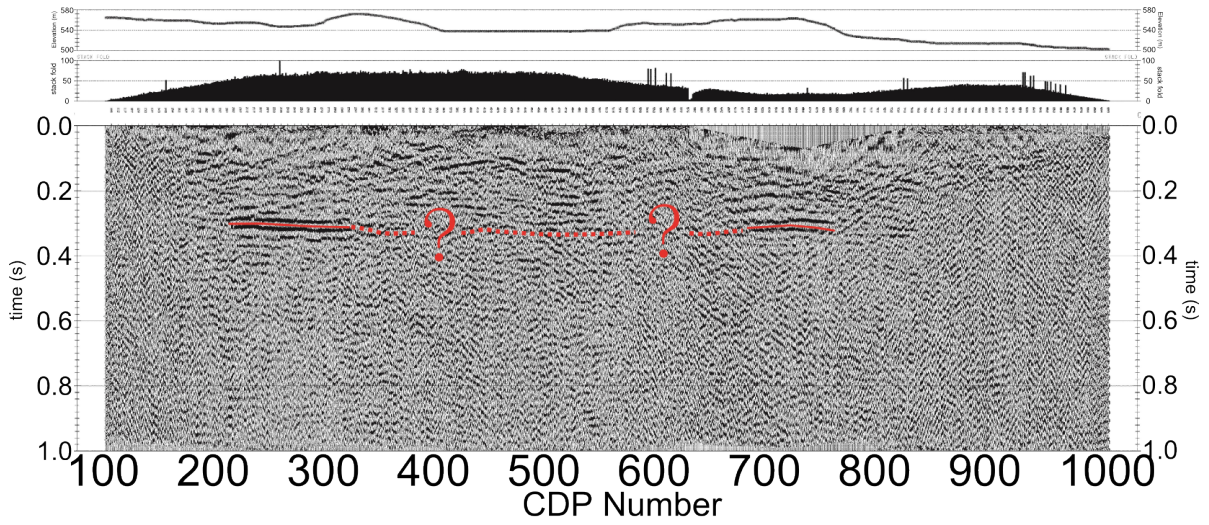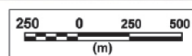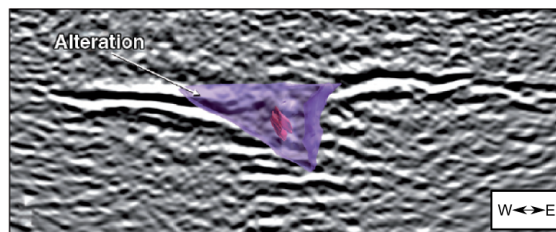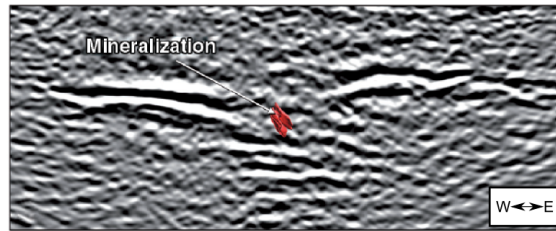
Figure 1.4: a) A CDP stacked profile along high-resolution line No.14 near the McArthur River Mine (White, 2007) b) Representative depth section from the migrated 3D 3C seismic data from Millennium, without (upper) and with (lower) the interpretation of alteration zone. The red zone is the ore body (Juhojuntti et. al. 2012).
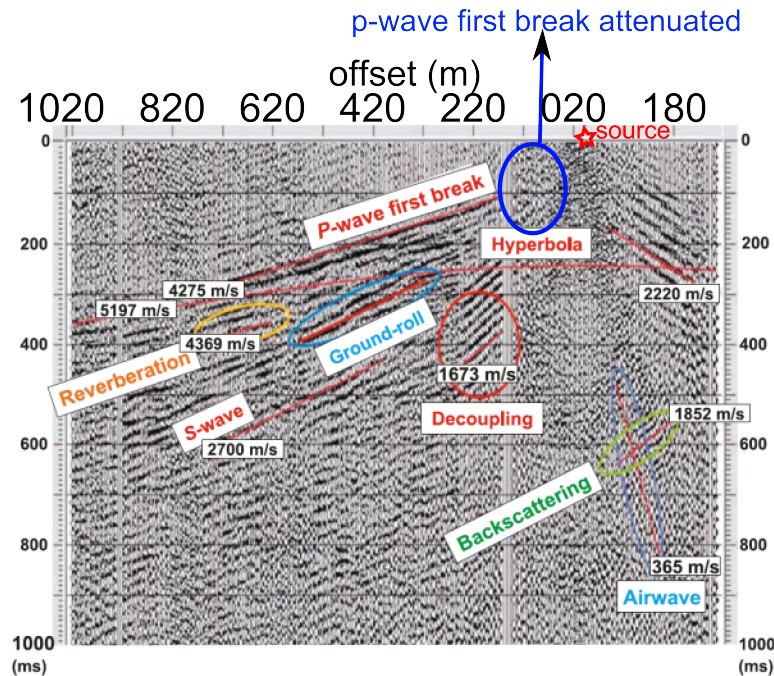
Figure 1.5: A raw common-source gather from the McArthur River surface seismic survey (Hajnal, 2010).

tion of seismic sections will be potentially improved by applying sophisticated processing and inverting methods. Chapter 2 of the report focuses on the amplitude versus offset/incident angle (AVO/AVA) calculation for the reflectivity of the unconformity. The effects of variable p- and s-wave reflectivity on the seismic data will be discussed. Chapter 3 introduces a method of estimation of s-wave velocity from the existing geophysical borehole measurements in the Athabasca Basin, which will provide basic petrophysical information for the s-wave processing of the seismic data. Chapter 4 displays and analyses the results of both the near- and offset VSP surveys acquired at McArthur River, especially focuses on the existence of s-wave. Chapter 5 shows and discusses the results of the 2D elastic and viscoelastic waveform modelling, which is conducted by the software package SOFI2D (Bohlen, 2002). Chapter 6 concludes and summarizes the results. Appendix A provides suggestions and general discussion of processing and inverting methods of the seismic data for uranium exploration in the Athabasca Basin, among which, the reverse-time migration forward modelling examples are given.

Chapter 2

Incident-angle-dependent reflectivity

2.1 The Zoeppritz equation and reflectivity

As p-wave sources dominant seismic surveys, seismic exploration focuses mostly on the condition of the incident p-waves. Figure 2.1 illustrates the situation when down-going p-wave encounters an impedance-changing interface. The products are reflected p-wave, converted s-wave, transmitted p-wave and transmitted s-wave. The angles of each of the products are given by the Snell's Law:

$$\frac{v_{pa}}{\sin\theta_1} = \frac{v_{pb}}{\sin\theta_2} = \frac{v_{sa}}{\sin\phi_1} = \frac{v_{sb}}{\sin\phi_2} = p \tag{2.1}$$

where v_{pa} and v_{pb} are p-wave velocities for upper and lower media, respectively. v_{sa} and v_{sb} are s-wave velocities for the upper and lower media, respectively. Incident and reflected p-wave have the same angle as θ_1, and θ_2 is the angle of the transmitted p-wave. phi_1 and ϕ_2 are reflection and transmission angle of s-waves, respectively. p is the ray parameter.

The distribution of wavefield energy on each product is given by the Zoeppritz Equation:

$$\begin{bmatrix} R_p \\ R_s \\ T_p \\ T_s \end{bmatrix} = \begin{bmatrix} -\sin\theta_1 & -\cos\phi_1 & \sin\theta_2 & \cos\phi_2 \\ \cos\theta_1 & -\sin\phi_1 & \cos\theta_2 & -\sin\phi_2 \\ \sin 2\theta_1 & \frac{v_{pa}}{v_{sa}}\cos 2\phi_1 & \frac{\rho_b v_{sb}^2 v_{pa}}{\rho_a v_{sa}^2 v_{pb}}\cos 2\phi_1 & \frac{\rho_b v_{sb} v_{pa}}{\rho_a v_{sa}^2}\cos 2\phi_2 \\ -\cos 2\phi_1 & \frac{v_{sa}}{v_{pa}}\sin 2\phi_1 & \frac{\rho_b v_{pb}}{\rho_a v_{pa}}\cos 2\phi_2 & \frac{\rho_b v_{sb}}{\rho_a v_{pa}}\sin 2\phi_2 \end{bmatrix}^{-1} \begin{bmatrix} \sin\theta_1 \\ \cos\theta_1 \\ \sin 2\theta_1 \\ \cos 2\phi_1 \end{bmatrix} \tag{2.2}$$

where R_p and R_s are reflection coefficients, and T_p and T_s are transmission coefficients of p- and s-waves respectively. ρ_a and ρ_b are densities of the upper and lower media. In the case of forward study with given velocity and density of the media, and the incident angle of the down going p-wave, the amplitudes of reflected p-waves and converted s-wave can be calculated by solving both Snell's and Zoeppritz equations.

Although the numeric calculation of reflectivity can be conducted by directly solving the Zoeppritz equation, the relationship between reflectivity and rock physical properties will become apparent while applying approximation methods. For reflected p-waves, one commonly seen form of the approximation of the Zoeppritz equation is the simplified Shuey's equation (Hilterman, 1989):
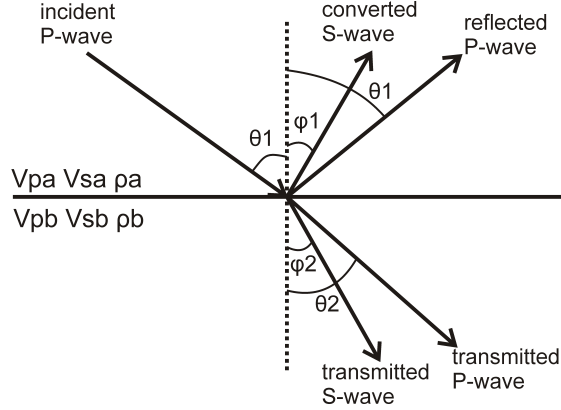
Figure 2.1: The four products (transmitted p- and s-waves, converted s-waves and reflected p-waves) generated when an incident p-wave encounters an interface.

$$R_p \approx \frac{I_2 - I_1}{I_2 + I_1} \cos^2 \theta_1 + \frac{\sigma_2 - \sigma_1}{1 - \frac{\sigma_2 + \sigma_1}{2}}^2 \sin^2 \theta_1 \qquad (2.3)$$

where $I_1 = v_{pa}\rho_a$ and $I_2 = v_{pb}\rho_b$ are acoustic impedances of the upper and lower media, respectively. σ_1 and σ_2 are Poisson's ratios of the upper and lower media that (Mavko, 2009):

$$\sigma = \frac{0.5 - \left(\frac{v_s}{v_p}\right)^2}{1 - \left(\frac{v_s}{v_p}\right)^2} \qquad (2.4)$$
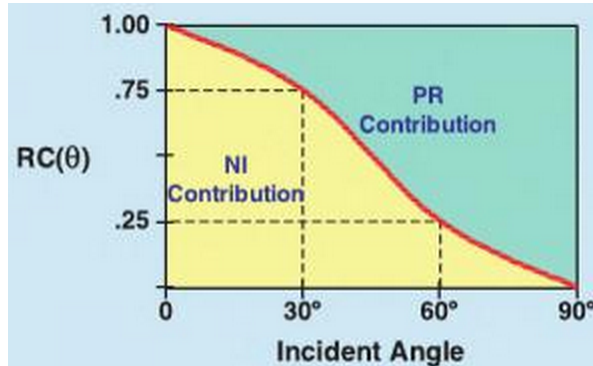
Figure 2.2: A general case of contribution of the acoustic impedance (NI) and the Poisson's ratio (PR) to the p-wave reflectivity versus incident angle predicted by the Hilterman's relationship (Hilterman, 1989).

Figure 2.2 illustrates the general relationship between the contribution of acoustic impedance (NI) and Poisson's ratio (PR) to the p-wave reflectivity versus incident angle. When incident angle is small, the second term of simplified Shuey's equation is insignificant. Thus, the p-wave reflectivity is dominantly controlled by the acoustic impedance. An extreme case would be the normal incidence, when neither s-wave is converted nor s-wave velocity has effect on the reflection coefficient. At large incident angle (>30°), the p-wave reflectivity is controlled by both the acoustic impedance and the Poisson's ratio.

The latter becomes increasingly dominant with increasing incident angle. A practical significance of the relationship is that the offset of seismic survey is required to be large enough for the AVO behaviour to be preserved, which is the case of the seismic exploration survey at McArthur River in the Athabasca Basin where the maximum offset is approximately 2.5 km for each shot.
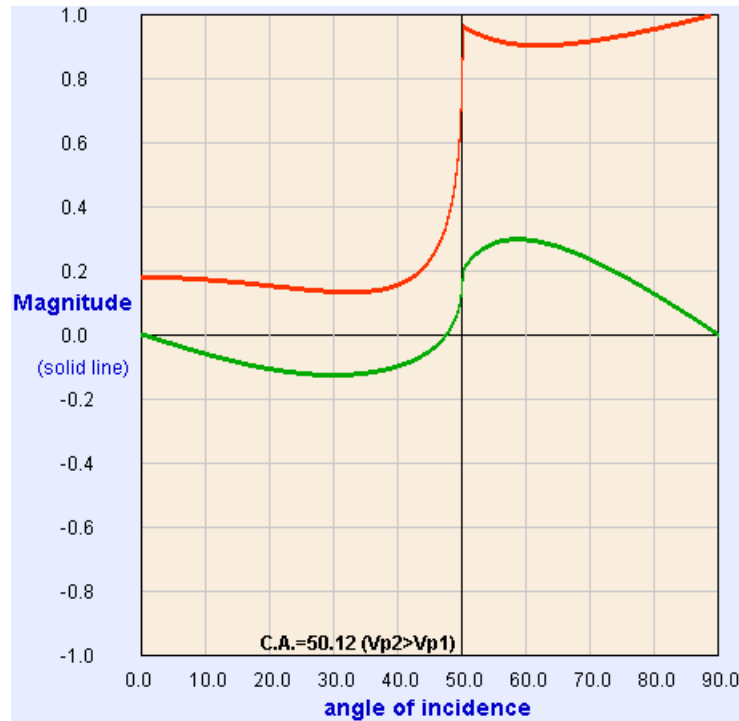
Figure 2.3: A general AVO calculation of both p- and s-wave amplitudes with slight velocity increase model using the Zoeppritz equation. (CREWES, 2014).

Figure 2.3 shows a general case of p- (red line) and s-wave (green line) amplitude considering a velocity increase interface. For the velocity increase model, a critical angle is preserved at approximately 50°. When the incident angle is greater than critical angle, transmitted p-wave energy disappears, and total reflection occurs. The s-wave conversion is limited near zero offset and generally increases when incident angle increases until approximately 30°. With more wavefield energy converted, reflected p-wave energy generally decreases from the zero offset. The p-wave amplitude increases significantly when approaching the critical angle. This figure indicates that another significance of the large offset survey is to preserve the s-waves at large incident angles.

2.2 Reflectivity of basement unconformity in the Athabasca Basin

The rock physical properties such as p- and s-wave velocity and density can be used for solving the Zoeppritz equation. In the Athabasca Basin, borehole geophysical logging measurements have been collected by the Geological Survey of Canada and Cameco Corporation before the surface seismic survey performed. Mwenifumbo et. al. (2007) conducted a petrophysical analysis focusing on the demonstration of the p-wave reflectivity of the unconformity for conventional reflected p-wave method. Figure 2.4 shows a statistic result of all the borehole p-wave velocity and density measurements of the Athabasca Group sandstone obtained in the McArthur River area. The p-wave velocity occurs in the range from 3.5 to 6.5 km/s and is affected mostly by the silicification alteration condition. The density of the sandstone occurs in the range from 2.4 to 2.9 kg/m^3.

There are two major difficulties for estimating the angle dependent reflectivity of the basement unconformity using geophysical borehole logging measurements in the Athabasca Basin. One is that the rock property information of the basement rocks is limited. As the drilling of the boreholes ceased very soon after reaching the basement rocks and plugging is implemented, the geophysical logging tool does not normally go below the unconformity. Even with a few measurements collected, the data cannot be representative for not only the highly variable lithology but also the changing alteration conditions. White et. al. (2007) mentioned the p-wave velocity of basement rocks for calculation of acoustic impedance is estimated through Wyllie's (1956) time-average method. The estimation does not match well with the real logging data, for the Wyllie's method applies only for granular rocks and under the assumption of high confining pressure. Thus, the estimation of angle dependent reflectivity of the unconformity can only be done within a wide range of borehole measurements (v_p between 4.8 and 6.2 km/s, density between 2.68 and 2.80 kg/m^3).
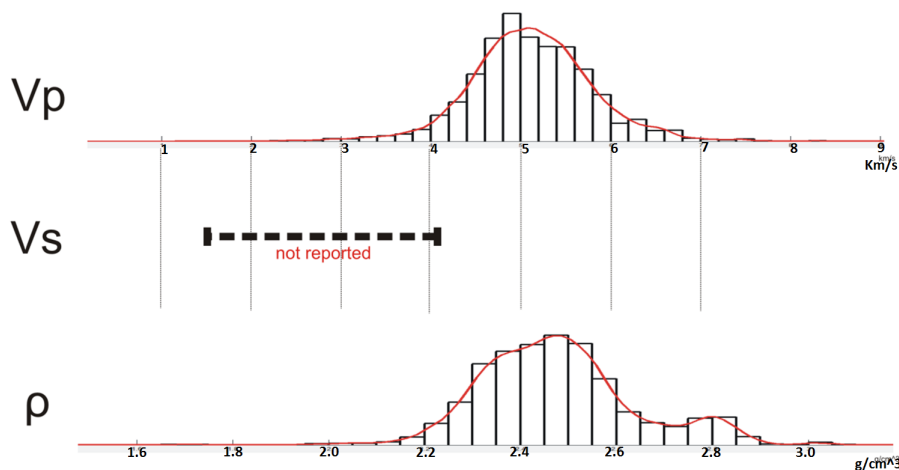
Figure 2.4: Statistics of borehole velocity and density measurements of the Athabasca group sandstone.

Another difficulty is that the s-wave velocity information is unavailable in the Athabasca Basin. The p-wave velocity is extracted from the sonic logs. Although s-waves are preserved in the data, they occur as a secondary event which is smeared by the first arrived p-waves. There are geophysical logging tools specially designed for measuring the s-wave velocity such as the Dipole shear Sonic Imager (i.e.

DSI, Schlumberger, 2014) that is recommended for any future borehole geophysical measurements in the Athabasca Basin. As yet, no literature has attempted to obtain s-wave velocity in the Athabasca Basin. The Chapter 3 of this report will provide a method of estimating s-wave velocity through the effective media approach. The s-wave velocity is estimated to range from 1.0 to 3.2 km/s for the Athabasca group sandstone. Because of the limited basement geophysical information, the estimation will neither be able to be conducted for the basement rocks, nor will be appropriate for non-granular rocks. Thus, the s-wave velocity of the basement rock for the reflectivity calculation is in the range from 1.2 to 4.0 km/s.
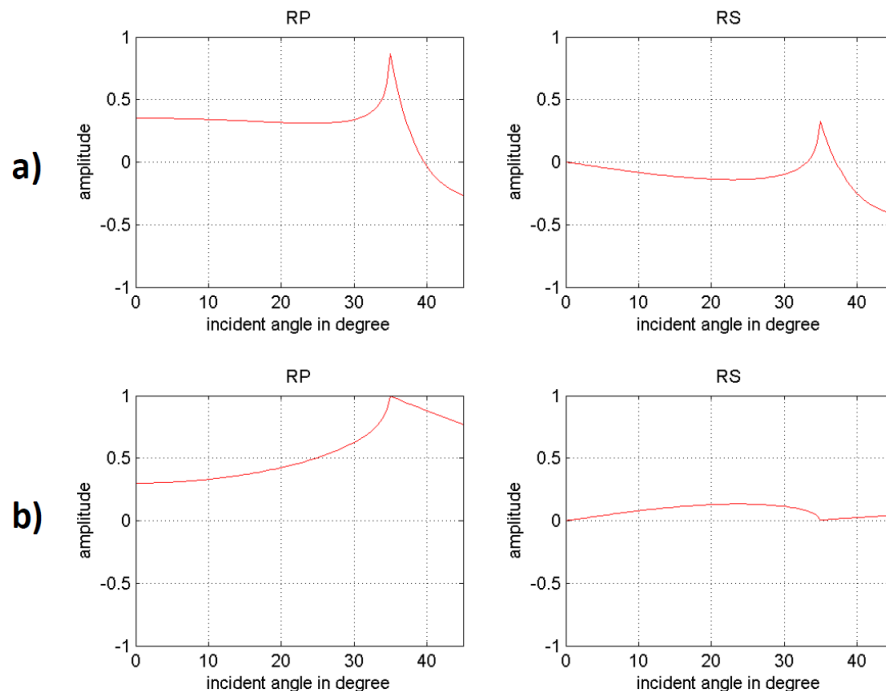
Figure 2.5: The AVO calculation of basement reflectivity of Athabasca group sandstone based on intense p-wave velocity increase assumption. a) p- (left) and s- (right) wave reflectivity for strong velocity contrast of both p- and s-waves. (Δv_p=3000 m/s Δv_s=2000 m/s). The Poisson's ratio in this case remains constant. b) only p-wave velocity contrast is strong (Δv_p=3000 m/s), s wave velocity contrast is negative and small (Δv_s=-200 m/s). The Poisson's ratio in this case increases significantly from 0.25 to 0.45.

The reflectivity is calculated for a couple sets of p- and s-wave velocity combinations, and plotted in 2-dimensional figures with x-axis being the incident angle and the y-axis being the amplitude. It is then calculated within the estimated range, and displayed in 3-dimensional figures with the third axis being a representative rock physical property (e.g. Poisson's ratio). For each of the results, only incident angle within $50°$ is taken into consideration.

Figure 2.5a shows the condition of both p- and s-wave velocities increasing intensely (both Δv_p and Δv_s >2000 m/s) from above to below the unconformity. The Poisson's ratio contrast is small. The p- and s-wave AVO behaviours are similar with the general situation shown in Figure 2.3. Because of strong acoustic impedance contrast, the zero-offset p-wave reflectivity is strong ($\approx$0.4), and there is no p-s conversion occurring. The p-wave reflectivity generally decreases, and s-wave reflectivity increases from zero offset when incident angle increases. When approaching the critical angle, p-wave reflectivity
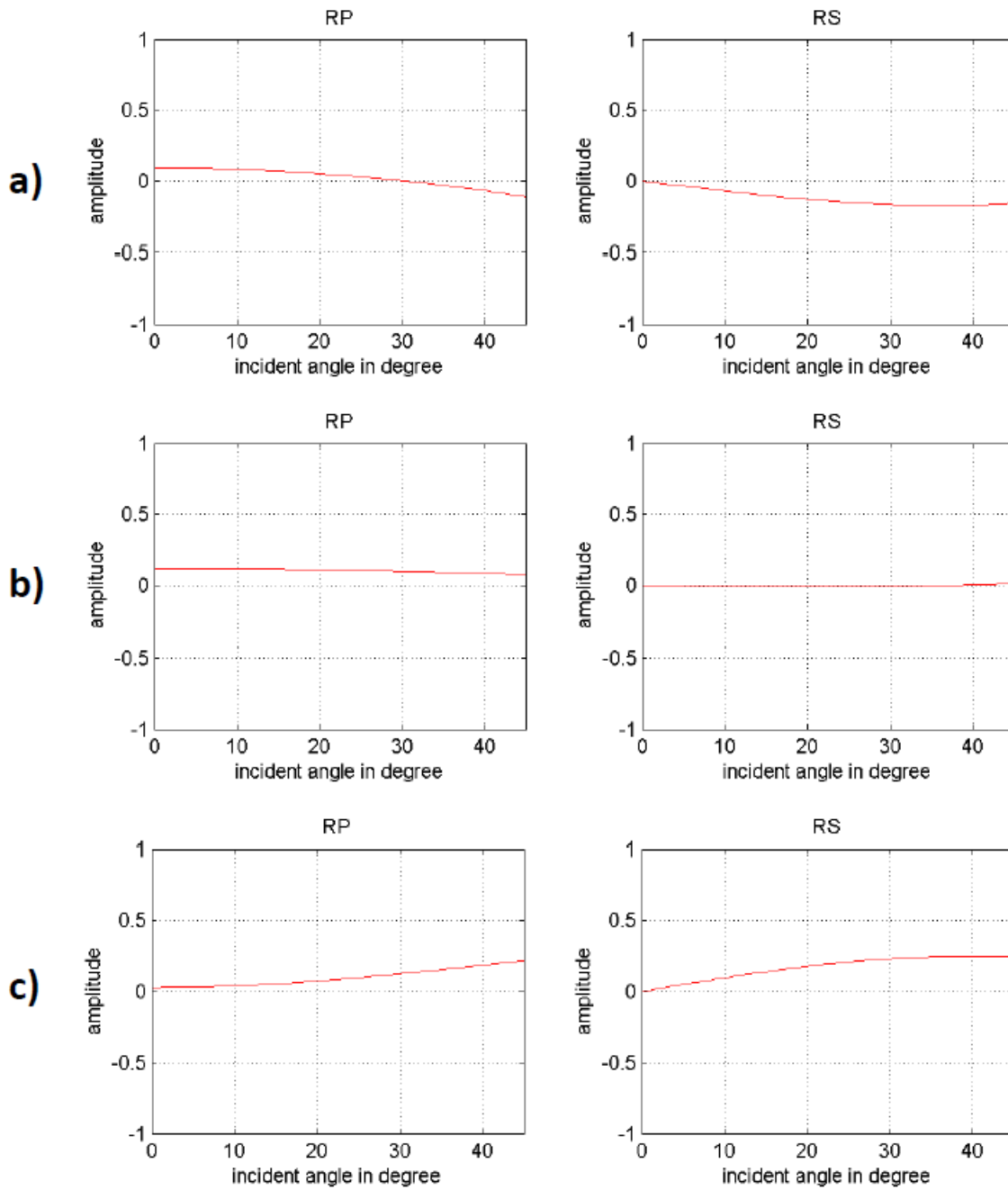
Figure 2.6: The AVO calculation of basement reflectivity of Athabasca group sandstone based on small p-wave velocity contrast assumption. a) p- (left) and s- (right) wave reflectivity for small velocity contrast of p-wave (Δv_p <200 m/s) and strong s-wave velocity increase (Δv_s=2000 m/s). The Poisson's ratio in this case decreases significantly from >0.4 to <0.2. b) Both p- and s-wave velocity contrast is small (Δv_p and Δv_s¡200 m/s). The Poisson's ratio in this case decreases slightly from 0.35 to 0.3. c) Small p-wave velocity contrast (Δv_p <200 m/s) with s-wave velocity decrease (Δv_s=-1000 m/s). The Poisson's ratio increases from 0.35 to 0.45.

experiences a sudden increase and s-wave reflectivity changes from negative to zero, and then to posi-
tive. Beyond the critical angle, both of the p- and s-wave reflectivity decrease fast and change phase.
With the same p-wave velocity of both above and below the unconformity, s-wave velocity can decrease
insignificantly, yielding a large positive Poisson's ratio contrast. The reflectivity calculation of p- and
s-waves is shown in Figure 2.5b. In this case, both the p- and s-wave amplitudes are positive. The
p-wave reflectivity increases monotonically before the critical angle, and the s-wave reflectivity raises
and then drops. The p-wave amplitude equals 1 at the critical angle, which denotes a total reflection
condition without either conversion or transmission.

The low acoustic impedance contrast (i.e. low p-wave velocity contrast) condition is one of the major
causes of the p-wave image loss in the Athabasca Basin. Figure 2.6 shows the reflectivity calculation based
on the assumption that p-wave velocity contrast is small (<200 m/s). Thus, the zero-offset reflectivity
is significantly small. Figure 2.6a shows the results of a strong s-wave velocity increase (>2000 m/s)
from above to below the unconformity preserved in an insignificant p-wave velocity contrast medium,
which yields a negative Poisson's ratio contrast. The p-wave reflectivity changes from the positive to
the negative when incident angle increases, and the s-wave reflectivity remains in the negative part and
increases continuously. When s-wave velocity contrast is also low (<200 m/s), the Poisson's ratio of the
upper and lower media remains constant. The reflectivity calculation is shown in Figure 2.6b. As each
elastic property contrast is very small in this situation, both p- and s-wave reflectivity remains small
regardless of incident angle changes. Most of the wavefield energy is transmitted rather than reflected.
If s-wave decreases from the upper to the lower media, the Poisson's ratio changes positively. Figure 2.6c
illustrates the reflectivity in this situation. Both of the p- and s-wave amplitudes in this case remain
positive, and display brightening character with increasing incident angle. The p-wave amplitude can be
much more significant than the zero-offset reflection even when p-wave velocity contrast is insignificant.

Considering the low p-wave velocity contrast condition, solving the Zoeppritz equation is conducted
for changing s-wave velocity contrast (Figure 2.7) and changing Poisson's ratio contrast (Figure 2.8).
When s-wave velocity contrast is small (Figure 2.7), p-wave reflectivity weakens at far offset shown as
Class 1 AVO response. With high s-wave velocity contrast (more than 2000 m/s), the AVO behaviour
of reflected p-wave turns into Class 2, which displays a phase changing character. Changing of s-wave
velocity contrast affect both reflected p-wave and converted s-wave AVO properties; however, converted
s-wave reflectivity remains in the negative phase within the velocity changing range.

Figure 2.8 shows the reflectivity calculations of p-p (left) and p-s (right) waves versus changing Pois-
son's ratio contrast. The black lines on the figure indicate where the reflectivity equals 0. Along the
unconformity where the p-wave velocity contrasts are small, faults and argillic alterations can signifi-
cantly decrease the s-wave velocity of the incident layer, resulting in greater Poisson's ratio in the upper
media but smaller in the lower (i.e. negative Poisson's ratio contrast). The reflected p-wave reflectivity
displays a phase changing AVO response at where the decrease of the Poisson's ratio is greater than
0.1. On the contrary, converted s-wave reflectivity either remains in the positive (with absolute value of
the Poisson's ratio contrast <0.1) or in the negative (with absolute value of the Poisson's ratio contrast
>0.2). In other words, the black line indicating reflectivity equalling 0 is almost parallel with the axis
of incident angle.
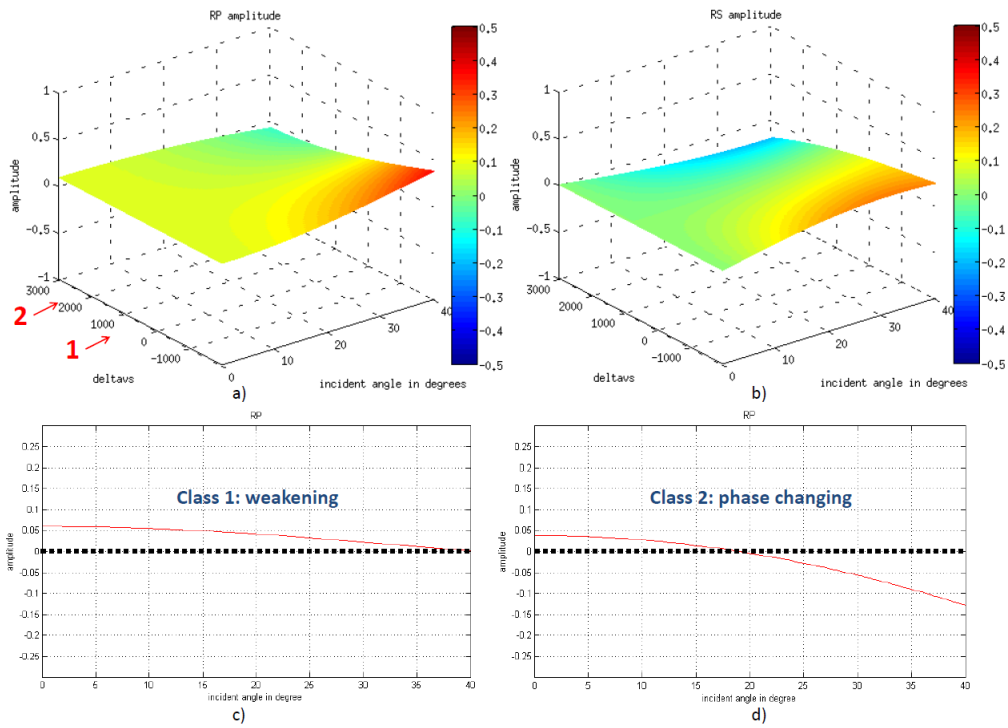
Figure 2.7: Calculated p- and s-wave reflectivity versus incident angle using Zoeppritz equation. The left horizontal axis is the Δv_s. a) and b) AVA response changes with s-wave velocity contrast. c) and d) AVA response class 1 and 2 as arrowed in a).
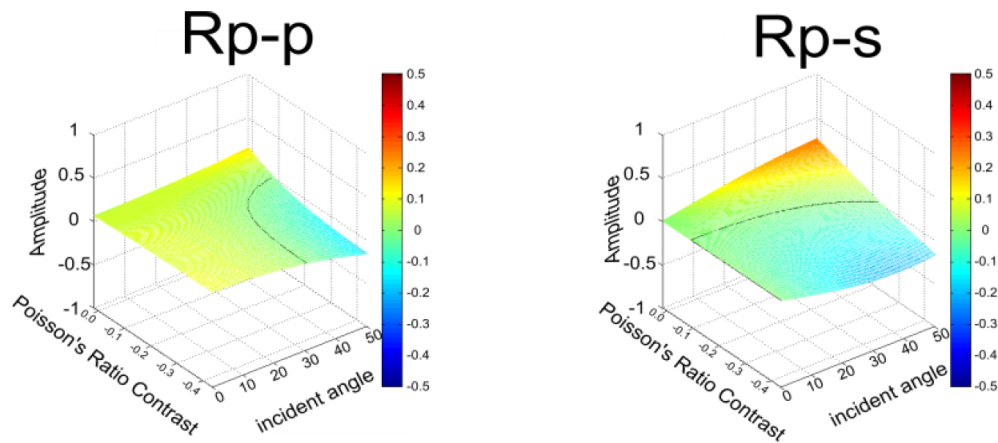
Figure 2.8: Reflectivity calculations of p-p (left) and p-s (right) waves based on the Zoeppritz equation. The model is based on a low p-wave velocity contrast condition (<600 m/s), and a wide range of s-wave velocity (1000-3200 m/s for upper layer and 1200-4000 m/s for lower layer). The Poisson's ratio contrast between the upper and lower layer is used as the axis for displaying the changing AVO trend. Black lines indicate where the reflectivity equals 0.

2.3   Variable reflectivity effects on the processing and interpretation of seismic data
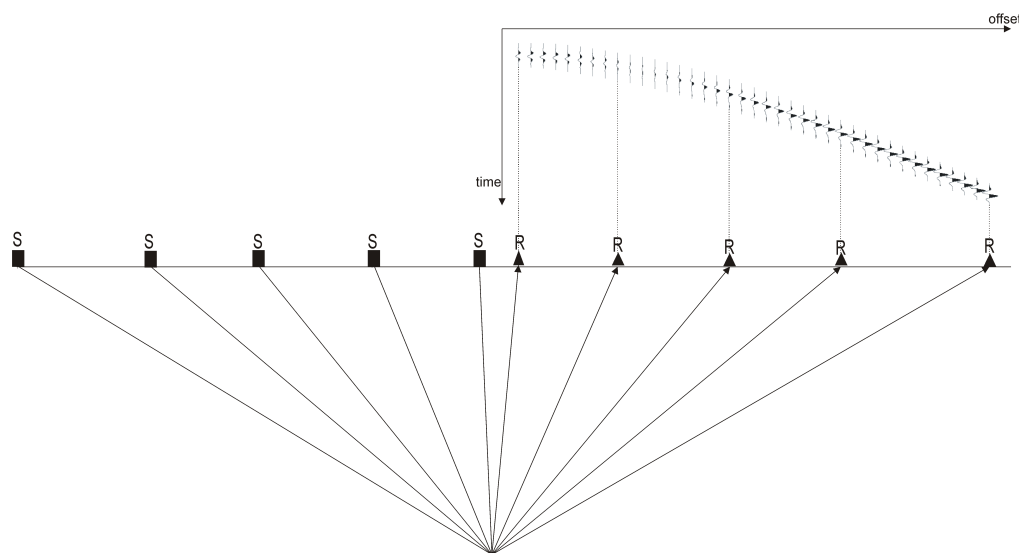
Figure 2.9: Source-receiver geometry of a CMP gather. Upper right shows a modelled trace with changing phase AVO response. The model is elastic. No compensation of geometrical spreading has been applied to the traces. Simply stacking these traces after NMO correction will result in a suppression of signals.

One of the major importances about the petrophysical and angle-dependent reflectivity study is that it suggests when conventional p-wave reflection seismic method fails. Common-midpoint (CMP) stacking is a major processing sequence of this type of seismic work. As shown by Figure 2.9, traces are sorted with respect to the same midpoint location of sources and receivers. Provided known velocity model, normal move-out (NMO) correction is applied to each of the traces to even up the event to the same time level (the zero-offset two-way travel time). The traces are stacked to enhance the signal and suppress the noise. An inherent assumption of the CMP stacking process is that the reflected event is theoretically in-phase. This is true for most of the high-impedance contrast cases because p-wave reflectivity will not experience a phase changing with large zero-offset reflectivity even when it is decreasing (Figure 2.5). When acoustic impedance is small, phase changing AVO response is common, especially when s-wave velocity contrast or Poisson's ratio contrast is large (Figure 2.6 and 2.7). The stacking of phase changing traces will result in a suppression of signals with each other and fail to image the target. This situation is one of the essential causes of image loss of the unconformity in the Athabasca Basin, and the 3D seismic data (Figure 1.4b) shows that it is more severe close to the mineralization zone.

When reflected p-wave fails to produce image of the unconformity, technologies are available considering other physical properties of the rock than the p-wave velocity or acoustic impedance. One example would be the AVO attribute analysis and inversion, which is common for low impedance contrast seismic data in the oil and gas industry. It utilizes the elastic impedance and Poisson's ratio accounting s-wave velocity to image the geological features (Hilterman, 1989). Another will be the imaging using converted s-wave in the seismic data. As shown previously, the converted s-wave almost has no phase changing character. The s-wave can be used for enhancing the image at where p-wave fails. For the processing of seismic data with considerations of preserving real amplitude, more velocity information

of the subsurface in the Athabasca Basin is essential. The next Chapter discusses an s-wave velocity estimation procedure by given the borehole geophysical logging data in the Athabasca Basin. The result can be applied for multicomponent 3D 3C data processing in the seismic project at Millennium.

2.4   Summary

The conventional reflected p-wave method images the subsurface features using the differences of acoustic impedance between different geologic materials. When p-wave velocity contrast is small, the acoustic impedance contrast is small, leading the fail of detecting signals on a zero-offset seismic section. At far offsets, both the p- and s-wave reflectivity are determined by not only the acoustic impedance, but also the Poisson's ratio that is correlative to both p- and s-wave velocities. Thus, a large maximum offset during the acquiring the seismic data is essential for the implementations of AVO attribute analysis and s-wave imaging.

For the uranium exploration in the Athabasca Basin, calculations of reflectivity based on the borehole geophysical logs suggests a very low p-wave velocity contrast above and below the unconformity, yielding a very low zero-offset reflectivity condition. Accompanying with the strong attenuation of seismic signal of the near surface materials, the reflected p-wave experiences difficulties in imaging the unconformity near the mineralization. With a significant s-wave velocity contrast, the expected p-wave AVO response tends to vary. The variation, once related to the lithology, can be used as a tool for AVO attribute analysis and inversion of seismic data in the Athabasca Basin. The s-wave AVO response at the relatively far offset tends to remain strong and in-phase, which allows the imaging by s-waves once extracted from the 3C seismic data at the Millennium area.

To achieve better image through s-wave and AVO methods, further petrophysical studies on s-wave velocities of the rocks in the Athabasca Basin are required. Measurements from the existing borehole using s-wave logging tool can be directly generated for the Athabasca Group sandstone. Laboratory experiments are also suggested for producing the s-wave velocity measurements on the basement rocks.

The reflectivity calculation conducted in this Chapter is informative and illustrative. The target unconformity depth is a few hundreds of meters in the Athabasca Basin. As the Zoeppritz equation is based on the planar wavefront assumption, which is not valid for the shallow seismic exploration, it cannot provide accurate amplitude estimations. To analyse AVO/AVA behaviour of the basement reflection in the Athabasca Basin, full elastic waveform modelling should be conducted.

Chapter 3

S-wave velocity estimation

3.1 The effective media approach and the Greenberg-Castagna method

The s-wave velocity can be useful for: 1) Forward modelling study with any non-acoustic (i.e. elastic and viscoelastic) assumptions. 2) Amplitude-versus-offset (AVO) reflectivity analysis as mentioned in the Chapter 2. 3) Processing and interpretation of multicomponent seismic data. Conventional borehole logging tools do not provide s-wave velocity information, so the s-wave velocity is not available in most places where the data was acquired early. This is the situation in uranium exploration at the Athabasca Basin, where the s-wave velocity cannot be extracted from the sonic logs as it is smeared by the first arrival. The logging data are collected by the Geological Survey of Canada and Cameco Corporation. The current uranium exploration study in the basin starts to involve with 3-dimensional and 3-component survey in Millennium, so the estimation of s-wave velocity is essential to assist the seismic work.
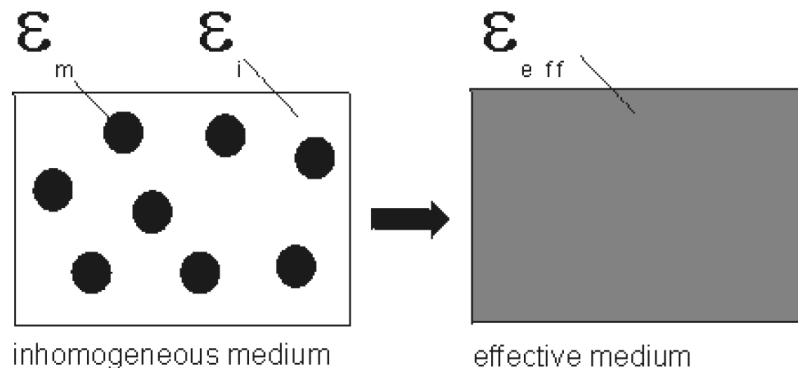
Figure 3.1: Illustration of effective medium theory. The theory neglects the inhomogeneity of the medium, and the effective medium has an effective modulus that is related to the modulus of the each constituent and its composition.

The estimation of s-wave velocity is commonly generated with two types of approaches: 1) empirical functions that consider the relationship among p-wave velocity, s-wave velocity, porosity and clay content etc. 2) estimation with petrophysical models through estimation of bulk and shear modulus (K and μ). The first approach is often based on abundant in-situ measurements either from boreholes or laboratories,

which is not currently available at the Athabasca Basin. The approach through petrophysical models can be done only with the presence of p-wave velocity, density measurements and assumptions.

The s-wave velocity estimation approach used in this chapter is based on the example given by Greenberg & Castagna (1992). The estimation results are given for the borehole MAC-218 from McArthur River area in the Athabasca Basin. Further studies on s-wave velocity estimation can be done by considering different approaches for the estimation of parameter in the petrophysical model.

The p- and s-wave velocities of a medium are characterized, respectively, by the following equations:

$$v_p = \sqrt{\frac{K + \frac{4}{3}\mu}{\rho}} \tag{3.1}$$

$$v_s = \sqrt{\frac{\mu}{\rho}} \tag{3.2}$$

where K is the bulk modulus, μ is the shear modulus and ρ is the density of the media. Each constituent of the media has its own shear and bulk modulus and density, which leads to rather complex conditions when p- and s-wave travel through. The effective media theory recognizes the media as one homogeneous and isotropic constituent macroscopically (Wang & Nur, 1992). The concept of effective media is illustrated by Figure 3.1.

The bulk modulus of a saturated rock consists of three components: K_{ma}, which is the bulk modulus of the grain matrix making up the solid part of the rock; K_{fl}, the bulk modulus of the fluid in the rock pore space, and K_{dry}, which is the bulk modulus of the dry rock skeleton. K_{ma} and K_{fl} can be directly acquired from laboratory experiments. However, K_{dry}, needs further estimation as it considers compression of the dry rock pore space component without compressing the solid grain, which is very difficult to achieve in the laboratory. As shear modulus of fluids is 0, the effective shear modulus of a saturated rock is equal to that of the dry rock, which does not provide sufficient information for estimation of shear wave velocity. The Gassmann's equation expounds the relationship among these components and the effective bulk modulus (Figure 3.2):

$$K = K_{dry} + \frac{\left(1 - \frac{K_{dry}}{K_{ma}}\right)^2}{\frac{\phi}{K_{fl}} + \frac{1-\phi}{K_{ma}} - \frac{K_{dry}}{K_{ma}^2}} \tag{3.3}$$

where ϕ is the porosity of the porous media, which is available through derivations of conventional logs (e.g. density, resistivity, velocity). The bulk modulus of the fluid can be found in literatures with lab experiments, and it does not vary considerably compared to that of the other components.

For a rock composed of a single mineral type, the bulk modulus of the solid grain (K_{ma}) would be equal to that of the mineral. For the solid part of the rock consisting of multiple minerals, K_{ma} is affected by volume percentage, size, shape and distribution of each mineral constituent. Thus, the estimation of K_{ma} is complicated and can be done mostly via estimating the range. This range is given by the Voigt's upper bound and Reuss's lower bound (Reuss, 1929):

$$Voigt : M_V = \sum_{i=1}^{N} f_i M_i \tag{3.4}$$
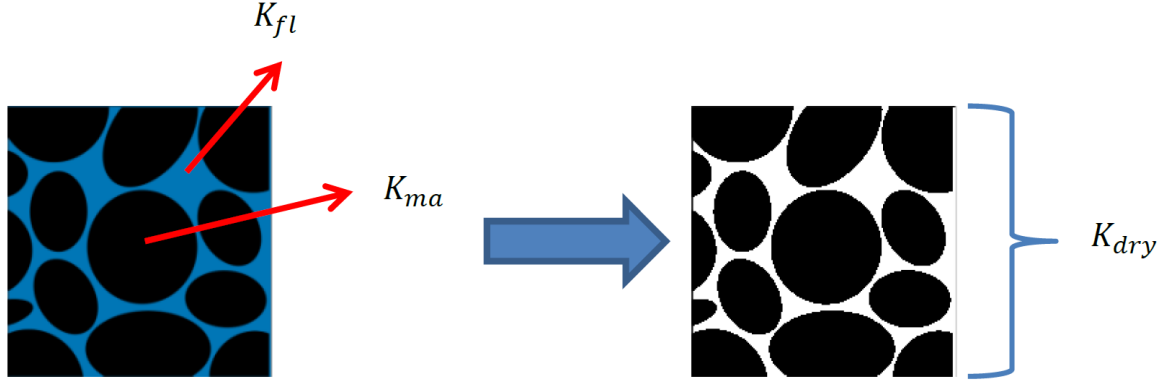
Figure 3.2: Illustration of each component of the effective bulk modulus of a rock saturated by a fluid. The effective bulk modulus consists of the bulk modulus of the fluid, the bulk modulus of the solid grain and the bulk modulus of the dry rock. The bulk modulus of the dry rock considers the incompressibility of the rock porous space only.

$$Reuss: \frac{1}{M_R} = \sum_{i=1}^{N} \frac{f_i}{M_i} \qquad (3.5)$$

M can be either bulk modulus or shear modulus. Notation V and R represents Voigt's upper bound and Reuss's lower bound, respectively. Notation i represents each rock constituent. f is the volume fraction of each component. Voigt's and Reuss's boundaries are derived assuming an equally distributed strain and stress on different constituents, respectively. Reuss's boundary effectively predicts the situation without confining pressure, which allows a precise estimation of fluid bulk modulus. Hill (1952) conducted estimation of modulus based on the arithmetic average of the Voigt's and Reuss's boundaries:

$$M_{Hill} = \frac{M_R + M_V}{2} \qquad (3.6)$$

Although the equation was created based on any mixtures, it is commonly used for estimation of bulk modulus of solid grains in the rock. The estimation of bulk modulus of the rock skeleton is difficult in most situations because the compression of the pore space commonly cannot be recreated through experiments. There are two ways summarized by Hilterman (2001): 1) the Greenberg-Castagna iteration method, and 2) the Biot parameter estimation.

The Greenberg-Castagna (1992) iteration method is based on the polynomial estimation of v_p and v_s relationship coupled with the Gassmann's equation (3.3). The iteration is solved by testing different water saturation to derive the closest results. For a saturated rock with known fluid bulk modulus, the first three steps described by Greenberg and Castagna directly give the result of bulk modulus estimation of the rock skeleton (i.e. K_{dry}).

Biot parameter is related to K_{dry} and K_{ma} by:

$$B = \frac{1 - K_{dry}}{Kma} \qquad (3.7)$$

where B varies from 0 to 1. B=0 indicates that the rock skeleton is completely compressed and further compression only affects the solid grains. B=1 represents the unconsolidated materials. For a rock under confining pressure, Biot parameter is estimated by Nur et al. (1991) as the ratio of porosity and critical porosity:

$$B = \frac{\phi}{\phi_{critical}} \tag{3.8}$$

where the critical porosity ($\phi_{critical}$) is the maximum porosity a rock can possess under confining pressure (i.e. the media will lose grain-grain contact with greater porosity), and it is an inherent parameter for a certain type of rock. Common value of critical porosity for sandstone is 0.4.

These two equations correlate K_{dry} to the porosity measurements of the rock.

3.2 Estimation for borehole MAC-218
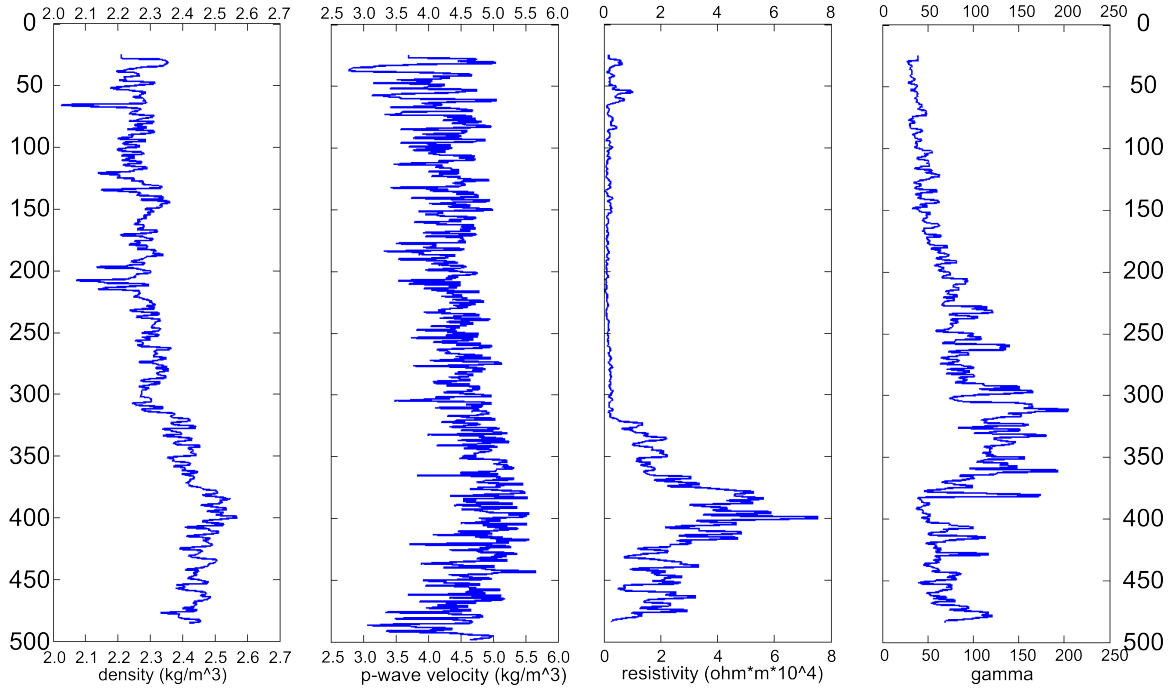
Figure 3.3: Major geophysical logs from borehole MAC-218 providing information for shear wave velocity estimation. From left to right: density, p-wave velocity, resistivity, and gamma.

I complied MATLAB (© The MathWorks, 2014) codes for estimating s-wave velocity using borehole logging data, that can be applied to any borehole data at the Athabasca Basin. The result from the borehole number MAC-218 (Figure 3.3) is given and discussed in this section.

The bulk modulus of the rock matrix (K_{ma}) is estimated using the V-R-H method. The estimating approach considers the model of the media is composed of three constituents: clay and quartz solid mineral grains and brine, which is a fully brine saturated with clayey sandstone. The clay content needs to be generated for s-wave velocity estimation because V-R-H and Greenberg-Castagna's estimation both require volume fraction of each constituent. The volume fraction of clay minerals can be estimated from the gamma ray log using the gamma index:

$$I_{gamma} = \frac{GR_{log} - GR_{min}}{GR_{max} - GR_{min}} \approx V_{clay} \tag{3.9}$$

where the GR_{log} represents the log measurements on natural gamma, GR_{min} and GR_{max} represents

the minimum and maximum in-situ gamma ray measurements. The porosity of the rock can be derived from either the density or the resistivity log, and it provides the volume fraction of brine as the rock is fully saturated. The porosity is derived from the density using:

$$\phi = \frac{\rho - \rho_{matrix}}{\rho_{fluid} - \rho_{matrix}} \tag{3.10}$$

where the matrix density is 2.65 g/cm^3 for typical sandstones and the fluid density is 1.01 g/cm^3 for brine. The porosity is derived from the resistivity using the Archie's equation:

$$\phi = \left(\frac{a * r_{fluid}}{r}\right)^{\frac{1}{m}} \tag{3.11}$$

where a=2.5 and m=1.57 for highly fractured sandstone, and fluid resistivity is 40 $\Omega \cdot m$ for brine (Sun, Milkereit and Schmitt, 2009).
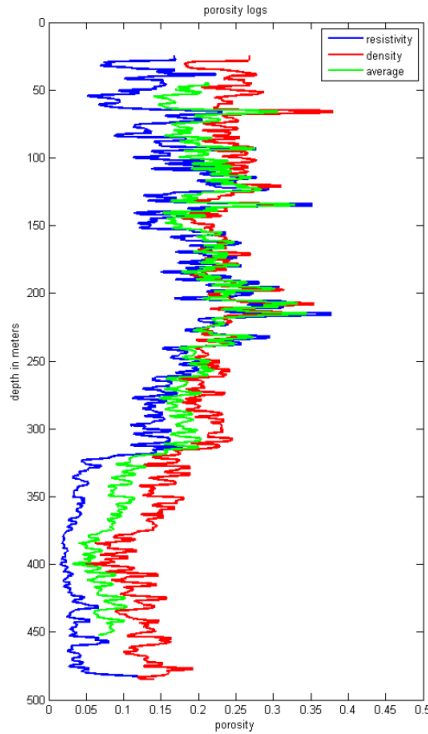
Figure 3.4: Derived porosity logs from resistivity log (blue) and density log (red). The resistivity log uses Archie's equation. The porosity used in v_s estimation is the arithmetic average of both derived porosities (green). The near-surface and near-basement samples in the log were cut to acquire better results.

Both porosities derived have their own limitations, especially when a material contains clay. Thus, the porosity used in the v_s estimation is the arithmetic average of the two derived porosities which is displayed in Figure 3.4.

The volume fraction of sand can be then derived by:

$$V_{sand} = 1 - V_{clay} - \phi \tag{3.12}$$

The bulk modulus of the sand-clay mixture solid grain is estimated using the V-R-H method (Figure 3.5). The bulk modulus of sand used is 37 Gpa, and that of clay is 20 Gpa. Measurement at each depth is treated as one rock sample. Thus, K_{ma} versus depth is derived (Figure 3.5 right).
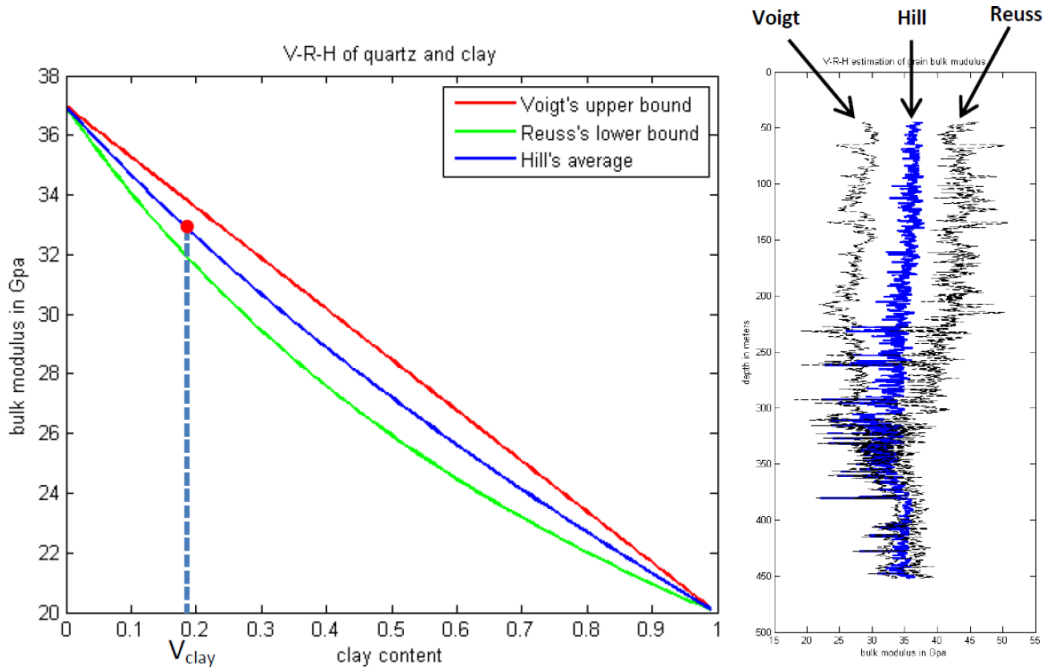
Figure 3.5: The V-R-H plot of a clay-sand mixture (left) and the V-R-H estimation of the bulk modulus of the solid grain in the borehole MAC-218 (right). The measurements of gamma ray provide the volume fraction of clay. Each depth is treated as one sample.

The Greenberg-Castagna estimation is based on the polynomial relationship between v_p and v_s:

$$v_s = 0.5 \left(\left\{ \sum_{i=0}^{L} V_i \sum_{j=0}^{N_i} a_{ij} v_p^j \right\} + \left\{ \sum_{i=0}^{L} V_i \left[\sum_{j=0}^{N_i} a_{ij} v_p^j \right]^{-1} \right\}^{-1} \right) \tag{3.13}$$

where a is an empirical coefficient. Greenberg and Castagna (1992) suggested a_{i0}=-0.85588, a_{i1}=0.80416 and a_{i2}=0 for typical sandstones, and a_{i0}=-0.86735, a_{i1}=0.76969 and a_{i2}=0 for typical shale (clayey stones). The above equation can be displayed in the shear-modulus form. For the sand-clay mixture, it becomes:

$$\sqrt{\mu_{dry}} = 0.25\rho \left[\{V_{sand} (a_{1sand}v_p + a_{0sand})\} + \{V_{clay} (a_{1clay}v_p + a_{0clay})\} \right]$$
$$+ \left[\{V_{sand} (a_{1sand}v_p + a_{0sand})\}^{-1} + \{V_{clay} (a_{1clay}v_p + a_{0clay})\}^{-1} \right]^{-1} \tag{3.14}$$

where rho comes from the density log measurements. Because shear modulus of fluids is always 0:

$$\mu_{dry} = \mu \tag{3.15}$$

by applying the relationship among v_p, K and μ, the effective bulk modulus (K) of the saturated rocks can be derived. With K, K_{ma}, and K_{fl} known, K_{dry} can be derived from the Gassmann's equation. The v_s estimation result is displayed in the Figure 3.6.
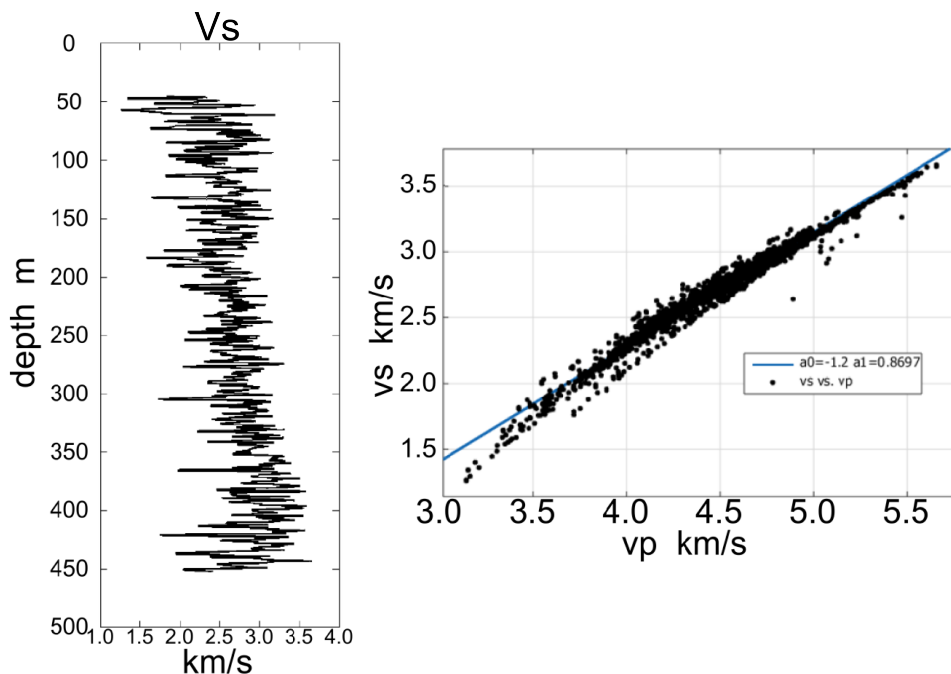
Figure 3.6: The v_s estimated using Greenberg-Castagna method (left) and $v_s - v_p$ cross plot (right). A polynomial fitting is displayed on the cross plot.

3.3 Summary

Logging from borehole MAC-218 is a representative example of subsurface conditions in the Athabasca Basin. The porosity of the sandstone above 300 m can be as high as 30% (Figure 3.4), which is responsible of the strong attenuation of seismic wave energies. At > 300 m, alteration begins to take place. Porosity decreases with an increasing clay content (gamma log from Figure 3.3), which causes the reducing of velocity contrast with the basement rocks.

The shear wave velocity is successfully derived from the local borehole log MAC-218, during which the density and resistivity log provide porosity information, and the gamma ray log provides the volume fraction of clay in the sandstone. The v_s is estimated to occur in the range of from 1.3 to 3.8 km/s. The v_s result in Figure 3.6 varies with a similar trend as v_p (Figure 3.3). The linear relationship between v_s and v_p is estimated by the $v_p - v_s$ cross plot (Figure 3.6 right), which can be used to generate further iteration processes in the Greenberg-Castagna method. The linear relationship between v_s and v_p, however, can be strongly effected by anisotropic conditions in the local highly fractured Athabasca sandstone. Further work on s-wave velocity estimation can be performed by considering the anisotropy, by comparing the Greenberg-Castagna method with others (e.g. Boit parameter method), or by considering clay effects on the porosity estimations.

The borehole No. MAC-218 is located right at the mineralization on the high resolution seismic line 14 in McArthur River area, and it is where the VSP survey takes place. Thus, it is considered as an representative example of the velocity estimation. Using the s-wave velocities generated above, a forward modelling study with an elastic assumption can be conducted, which will be discussed in Chapter 5. The estimated velocity can also be implemented into the AVO reflectivity analysis as described in Chapter 2. By applying the estimation for borehole data in the Millennium area, basic s-wave velocity information

for 3C seismic data processing is known.

Chapter 4

S-wave observed in the VSP data

4.1   Raw data

Figure 4.1: Photos taken during the acquisition of VSP data in winter 2001. Upper left is the downhole acquisition tool. Upper right is the vibrator track. Lower is the junction box.(Wölz & White, 2001)

For the high resolution seismic survey conducted in the McArthur River area, only vertical component geophones are used to record data. Converted SV waves can be recorded at far offsets, as the particle motions partially exist in the vertical direction. Figure 1.5 shows an s-wave event marked on the common shot gather. An apparent linear move-out velocity of 2700 m/s is given. This does not give the exact s-wave velocity because even the hyperbola is an approximation for a converted s-wave event when the reflecting interface is horizontal, and the time of the event cannot be defined accurately on the noisy shot gather.

In February 2001, both of a near and offset VSP surveys were generated in the borehole MAC-218 in the McArthur River area (Figure 1.2). The seismic data was recorded by 3-component geophones. Figure 4.1 shows pictures of the 3-component downhole seismic tools, the vibrator truck and the junction box used for the VSP survey. Table 4.1 summarizes the acquisition parameters for the high-frequency VSP survey. The data was acquired covering the depth from 60 to 460 m, which is ceased right above the local unconformity at 470 m depth analysed by Mwenifumbo (2007). The processing of VSP data was completed in the Geological Survey of Canada by Wölz & White (2001) in September. The processing results in the corridor stacked zero-offset standard traces used for assisting the p-wave surface seismic data interpretation in the McArthur River area.

Figure 4.2 shows plots of each component of raw data of the VSP survey, and Figure 4.3 is a zoom-in of the first 400 ms records. Records are AGC gained. For the near VSP, 156 traces with 2.5 m interval were acquired. The wavefield energy distributes almost equally on each of the component. First arrivals are well preserved on the vertical component record, which is useful for characterizing the p-wave direction on the VSP data. For the offset VSP survey, wavefield energy is more concentrated in the H2 component. The first arrivals are not only remained in the vertical component in this case, but also exist in the two horizontal components. The down-going wavefield energy are apparent on both of the near and offset VSP raw records.

Parameters	Near-offset VSP	Offset VSP
Source	Mini-Vibroseis	Mini-Vibroseis
Sweep frequencies	20-300 Hz linear upsweep	20-200 Hz linear upsweep
Sweep per VP	4-8	4-8
Source offset from collar	27m	326m
Receiver spacing	2.5m	5m
Depth range covered	60-460 m	60-460 m
Number of recording levels	156	80
Recording instrument	Oyo seismograph	Oyo seismograph
Downhole tool	4-level Vibrometrics	4-level Vibrometrics

Table 4.1: Acquisition parameters for both near and offset VSP surveys.

Near-offset VSP   Offset VSP
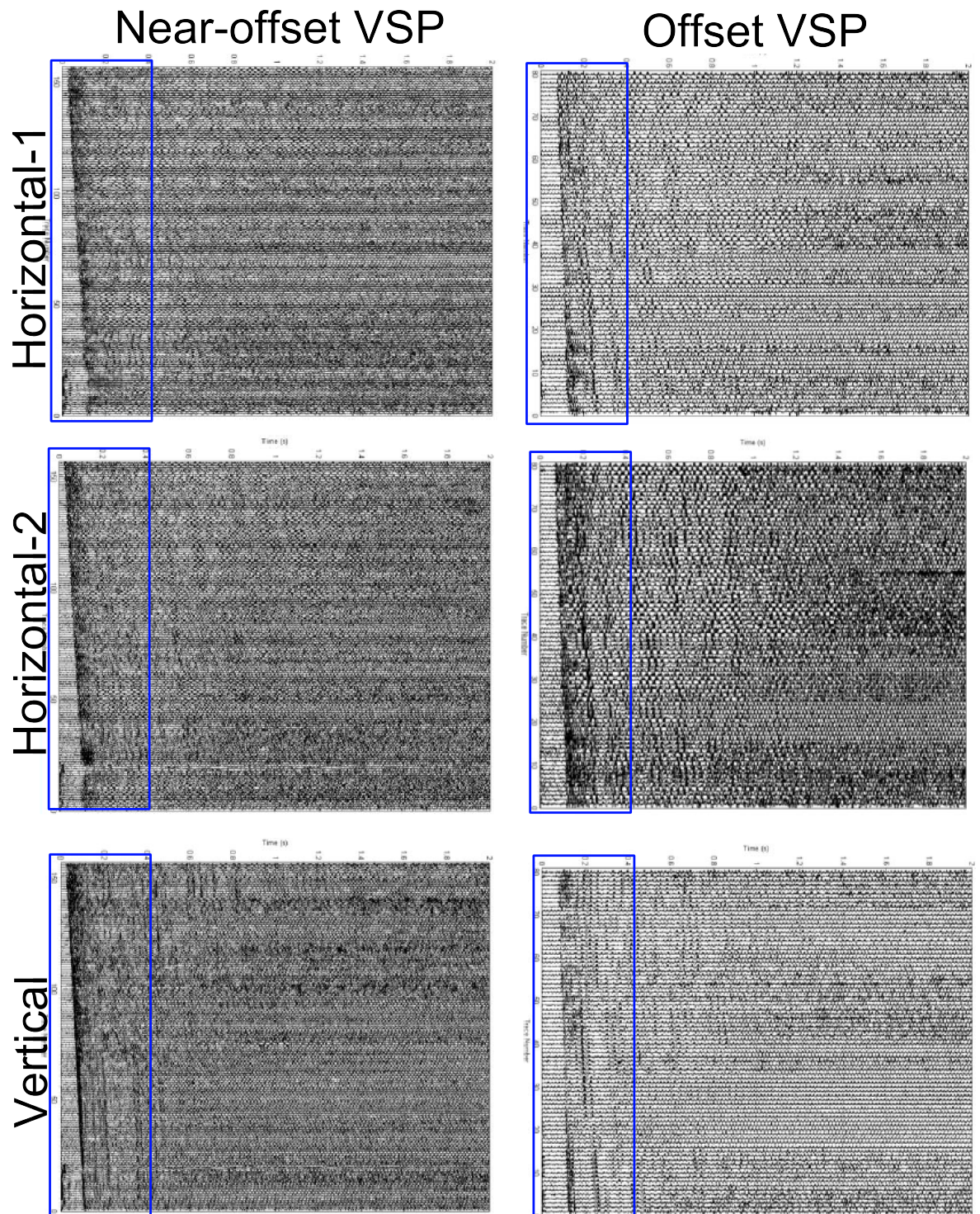
Figure 4.2: Each component of near and offset 3 component VSP raw data with AGC. Left: the near VSP data. Right: the offset VSP data. Upper: Horizontal-1 component. Middle: Horizontal-2 component. Lower: Vertical component. The blue box marks the window used to zoom-in into first 400 ms as shown in Figure 4.3

4.2   The rotation process

For a surface seismic survey, the s-wave is often separated into two components as SH and SV waves. As the p-wave intersects the surface perpendicularly, the particle motion of SV wave is pointing towards the source, and SH is perpendicular to the plane of SV and p-wave direction. The situation is different and more complex for the multicomponent VSP survey when the p-wave neither intersects the receiver line perpendicularly nor on the vertical direction. Figure 4.4 illustrates the relationship between the particle motion of the p- and s-waves and the receiver orientations for both near and offset VSP surveys. For the near-offset VSP, the particle motion of up-going reflected p-wave is on the vertical direction if the offset between the source and the uphole location is ignored. As the particle motion of s-wave is perpendicular to that of the p-wave, s-wave is on the horizontal plane. The two components of s-wave in this case are on the radial (SH-r, pointing towards the source) direction and on the transverse (SH-t, pointing into and out of page on Figure 4.4) direction, respectively. For the 3-componet VSP survey, the vertical direction is determined, and the other two horizontal directions rotate continuously in the borehole. Thus, the wavefield direction needs to be determined in the VSP data. For the near VSP case, the determination of SH-r and SH-t directions are rather simple, as wavefield needs to be only rotated on the horizontal plane (i.e. a 2D rotation). Moreover, as discussed in Chapter 2, converted s-wave energy is considerably small at the near zero-offset reflection for the near VSP survey. S-wave can be preserved in the near VSP data when the reflecting interface is not horizontal. For the offset VSP survey, the particle motion of reflected p-wave is distributed onto both vertical and radial horizontal directions. Thus, one component of the s-wave is also distributed onto vertical (SH-v, pointing vertically) and radial horizontal (SH-r, pointing towards the source) directions. The SH-t component remains the same direction as that of the near VSP survey. To completely separate the p- and s-wave energy, the wavefield needs to be rotated 3-dimentionally. Using the reflected p-wave, the other two s-wave directions can be determined. The rotation method is described by Daley et. al. (1988) using the operator:

$$
\begin{bmatrix} P \\ SV \\ SH \end{bmatrix} = \begin{bmatrix} \cos\phi & \cos\theta\sin\phi & \sin\phi\sin\theta \\ -\sin\phi & \cos\theta\cos\phi & \sin\theta\cos\phi \\ 0 & -\sin\theta & \cos\theta \end{bmatrix} \begin{bmatrix} Z \\ H_1 \\ H_2 \end{bmatrix}
\tag{4.1}
$$

where Z is the vertical component, and H_1 and H_2 are the two horizontal components, respectively. P is the wavefield component parallel to the p-wave particle motion. SV is the s-wave component with particle motion towards the source. SH is the other s-wave component. ϕ is the angle between P and Z direction, and θ is the angle between H_1 and SH direction. On one VSP trace, picking up the first arrival yields Z, H_1 and H_2 for the direct p-wave. For the p-wave first arrival, SV and SH are both 0. Thus, ϕ and θ can be solved for the direct wavefield. As the direction of SH wave are the same between direct and reflected events, the angle between H_1 and SH (θ) is constant. The angle between P and Z changes between the direct and reflected p-waves. The ϕ can be only determined by picking up the reflected p-wave event on the VSP data. With θ and ϕ known for the trace, P, SV and SH can be solved. This method of defining polarization of seismic events requires picking of p-wave reflections from the target unconformity instead of picking p-wave first arrival only, as they obtain different polarization directions.

According to the processing report of McArthur River VSP data (Wölz & White, 2001), both of the near and offset VSP surveys are rotated only on the horizontal plane. Thus, p-wave energy remains in the rotated horizontal component, and complete p- and s-wave separation is not achieved. As suggested
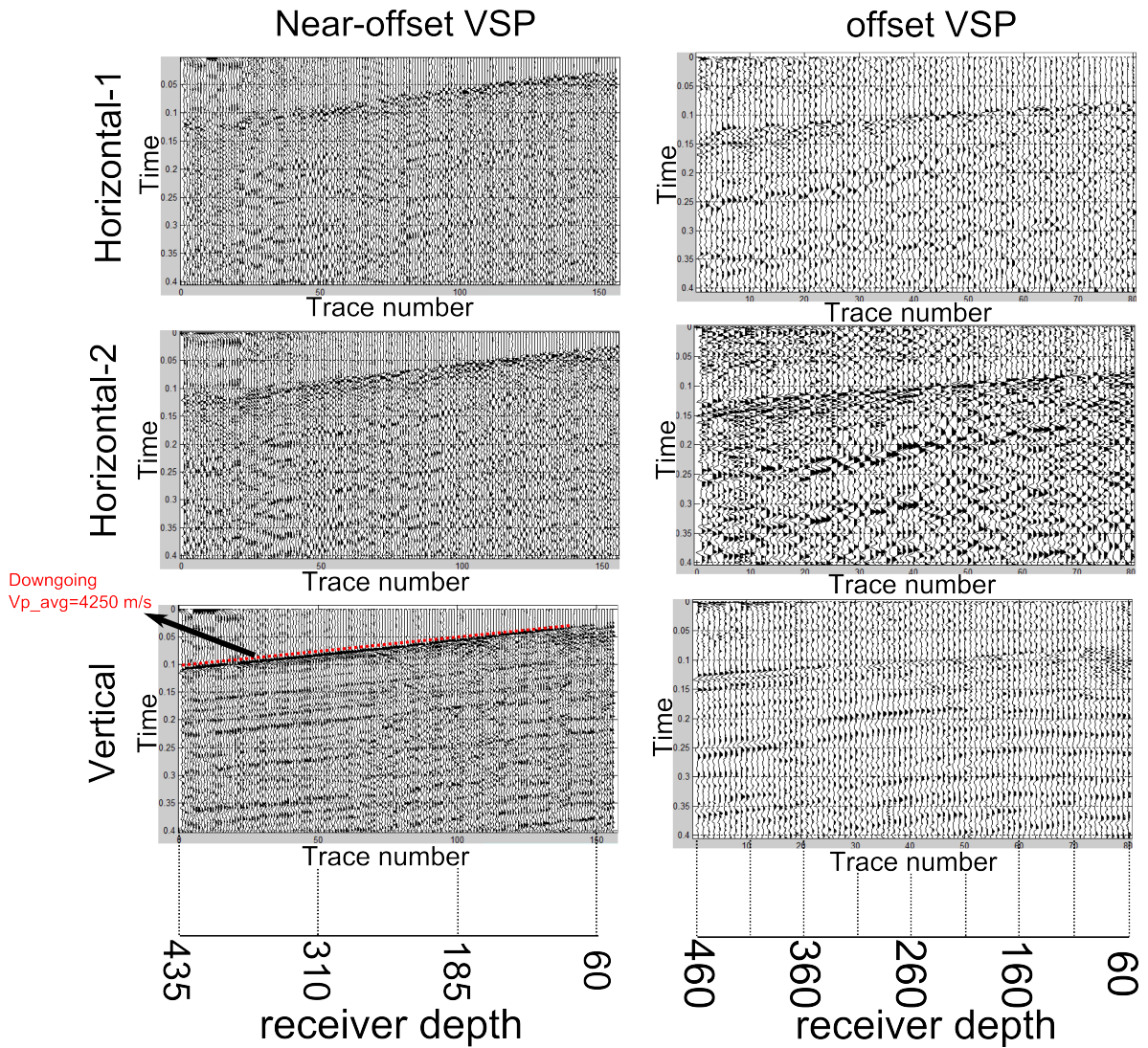
Figure 4.3: Zoom-in of first 400 ms of each component of both near and offset 3 component VSP surveys. Left: the near VSP data. Right: the offset VSP data. Upper: Horizontal-1 component. Middle: Horizontal-2 component. Lower: Vertical component.
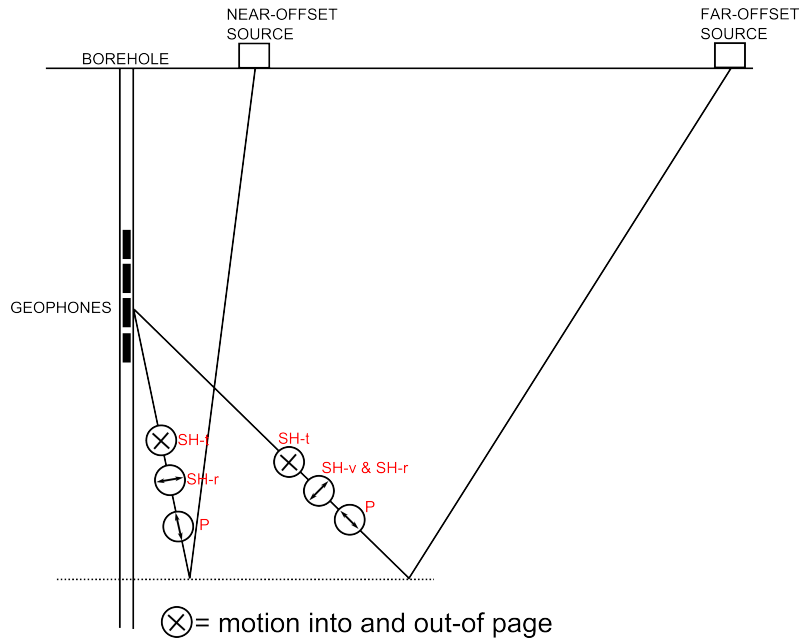
Figure 4.4: Illustration of polarization of reflected p- and converted s-wave events for both near and offset VSP surveys.
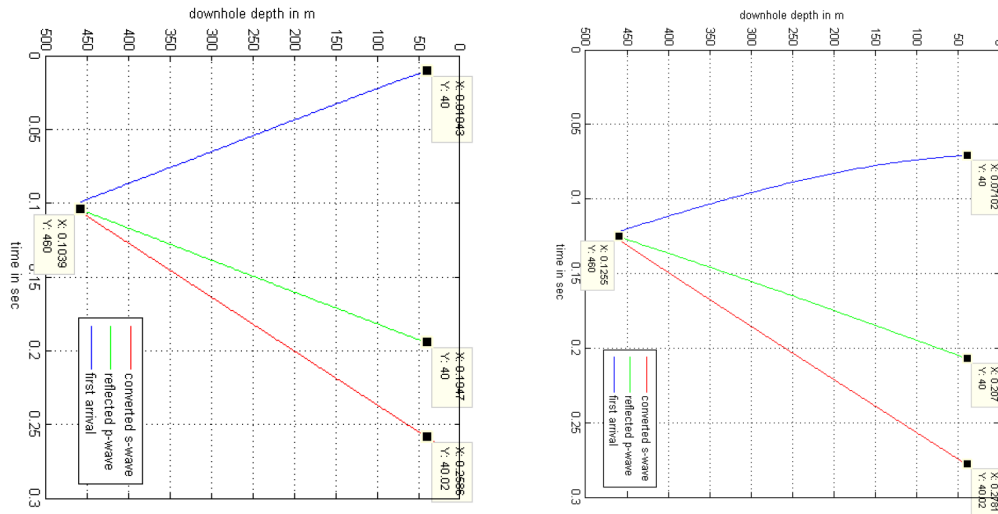
Figure 4.5: Estimated time-offset relationships for near (left) and offset(right) VSP surveys. Blue line represents the event of direct arrived p-waves. Green line represents the event of reflected p-waves. Red line represents the converted s-waves. Both p- and s- up-going events can be approximated using straight lines, as the source offset is small considering the acquisition depth for both surveys. The apparent velocity of the linear velocity thus represents the p- and s-wave velocity, respectively.

by the report, p-wave average velocity calculated by the first break is 4625 m/s, and s-wave velocity appears on the offset VSP data is 3290 m/s. Figure 4.5 is a calculation of both p- and s-wave time-offset relationships considering the VSP acquisition conditions. The first breaks are direct arrived p-waves that encounters the shallowest receiver first. According to the borehole analysis from Mwenifumbo (2007), the unconformity depth of borehole MAC-218 is about 470 m. With the deepest trace located at 460 m, which is right above the unconformity, the reflected p-wave and converted s-wave should intersect first break at that ending trace. For the near VSP survey, with only 400 m of depth coverage, the direct arrival, reflected p-wave and converted s-wave are all appear to be linear event. For the offset VSP survey, only first arrival changes to hyperbola. For both surveys, p- and s-wave can only be distinguished by the apparent linear velocity. On an incompletely separated 3-component data, the identification of p- and s-wave event is not always accurate.

The 2D rotation is applied on the horizontal plane (Wölz & White, 2001) (Figure 4.6). The wavefield energy considering the first break direction is maximized to the Horizontal-1 direction. This process, according to former discussion, spread p-wave and SV energy onto both Horizontal-1 and vertical directions, and SH energy remains on Horizontal-2 direction mostly.

The Vertical component remains the same before (Figure 4.3) and after (Figure 4.6) the rotation process. An average p-wave first arrival velocity is estimated to be 4250 m/s. Significant p-wave velocity increase can be observed through out the data. The direct p-wave arrives at the minimum offset receiver can be used to calculate the p-wave velocity of the near surface material (v_{p0}=2440 m/s. The p-wave velocity above 185 m depth is 4300 m/s, and below is 5150 m/s. The down-going s-wave can be observed on the Horizontal components of the offset VSP data. The s-wave in loose near surface material travels with extreme low velocity of 300 m/s. From 100 to 400 m depth, the s-wave velocity increases from 3300 m/s to 4150 m/s. On the vertical component of the offset VSP data, the ground-roll can be observed to the depth of approximately 110 m, suggesting that the overburden attenuates the seismic wave energy significantly.

4.3   Processing result—Up-going energy only

Following processing steps include median and fk filter removal of down-going wave energy, bandpass filter and AGC gain (Wölz & White, 2001). Figure 4.7 shows the first 500 ms of each component of both near and offset VSP data processed results. Identified events have been notified on the figure. For the near VSP data, as source is rather close to the borehole, p-wave energy on the horizontal plane is minor (see raw data in Figure 4.2). Thus, the characterization of p-wave orientation cannot be well achieved, which yields remaining of p-wave energy on the Horizontal-2 component. The reflected p-wave from the unconformity is most significant on the vertical direction, and also distinguishable on the Horizontal-1 and Horizontal-2 directions. The advantage of the near offset VSP survey is that the reflections within the Athabasca Group sandstone are clearly visible, which allow the building of p-wave velocity model above the unconformity. Converted s-wave energy cannot be identified on the near VSP data, as the incident angle of p-wave to the unconformity is close to zero. The lack of s-wave energy also denotes that the reflecting interface is majorly horizontal. For the offset VSP data, first arrived p-wave energy exists more on the horizontal plane (see raw data in Figure 4.2). Thus, the rotation delivers better results. On the Horizontal-2 component, reflected p-wave event cannot be identified. The up-going events within the sedimentary sequence for the offset VSP survey are not as significant as the near VSP. Converted s-waves from the unconformity are more identical than the reflected p-waves on the offset VSP data. The SV wave energy is distributed into both Vertical and Horizontal-1 components. On the Horizontal-2 component, as the p-wave energy is completely removed, a very distinct SH event can be identified through the entire record.

Comparison between the near and offset VSP data shows that p-wave energy decreases and s-wave energy increases with increasing incident angle to the basement unconformity in the borehole MAC-218. The s-wave velocity matches that suggested by the VSP processing report. For future analyses of s-wave in the VSP data, a complete 3D energy rotation is suggested to be applied on the data for achieving the separation of p- and s-wave wavefield. As SV and SH are both identical, the VSP data has the potential to be used for the anisotropic analysis of the rock property in the Athabasca Basin.

4.4   Summary

The unpublished processing steps of VSP data generated within the borehole No. MAC-218 are re-examined for the existence of s-waves. The down-going p- and s-waves are reviewed on each components of the VSP sections after rotation processes, and the up-going p- and s-waves can be observed after removal of down-going energy of the rotated sections. As the down-going s-wave propagating direction is oblique to the vertical direction, it cannot be observed on the vertical component VSP record on the near offset data. Because near-zero offset s-wave conversion is limited, the up-going s-wave can never be observed at the near offset VSP.

One distinct velocity increasing in the Athabasca Group sandstone is visible on the rotated VSP section, where the p-wave velocity changes from 4300 m/s to 5150 m/s and s-wave velocity changes from 3300 m/s to 4100 m/s. The strong s-wave velocity contrast yields an up-going s-wave event distinguishable on the vertical component of the rotated offset VSP data. The p- to s-wave velocity ratio remains steady between 1.2 and 1.3. On the contrary, the loosely packed surface overburden possesses significantly different petrophysical properties. As seen from the vertical component of the
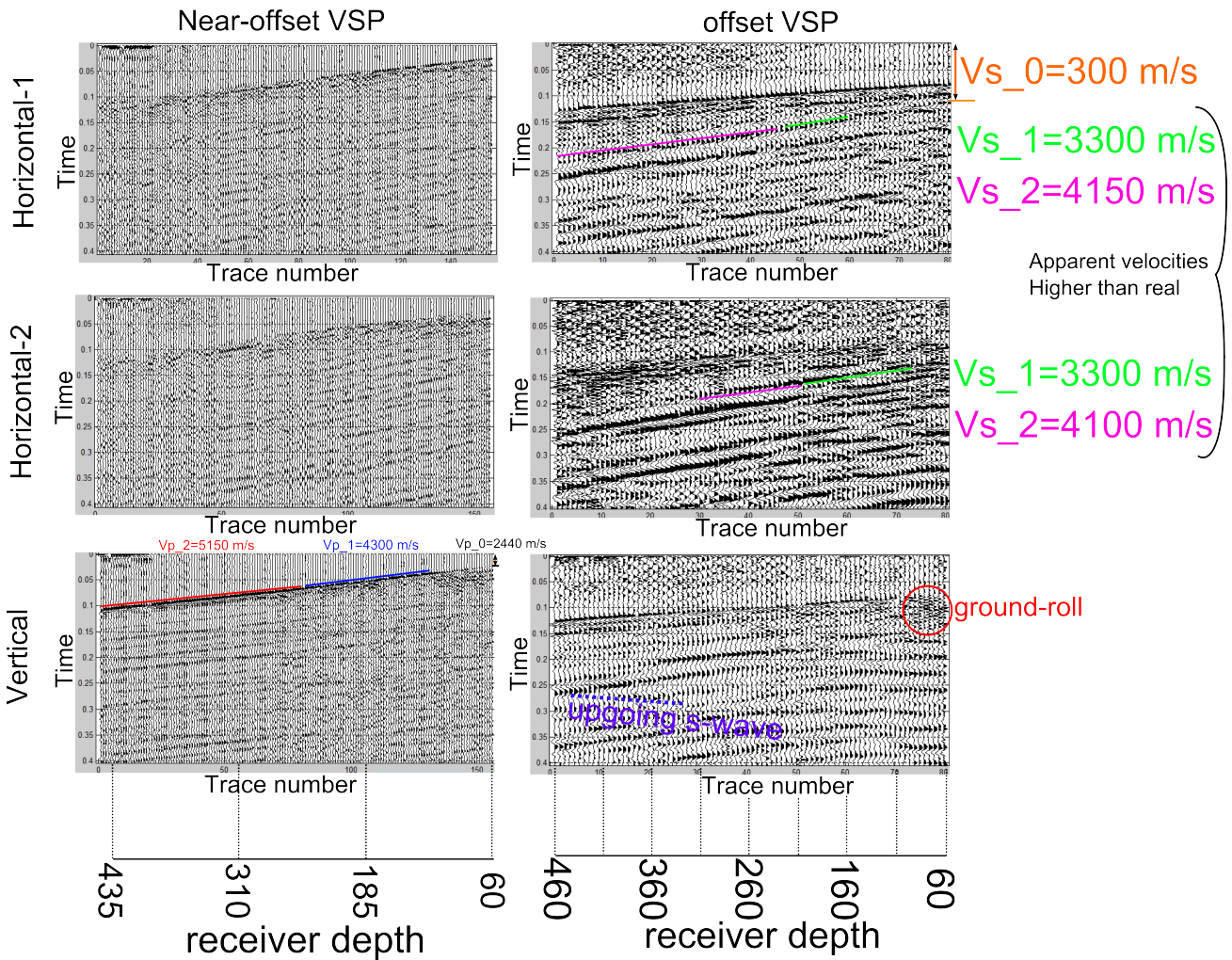
Figure 4.6: First 400 ms record of each component of both near and offset VSP surveys after rotation processing step. The rotation is conducted only on the horizontal components, and the vertical components of both near and offset record remain the same. All measurements are apparent velocities, and the real velocity is lower for s-waves considering propagating directions
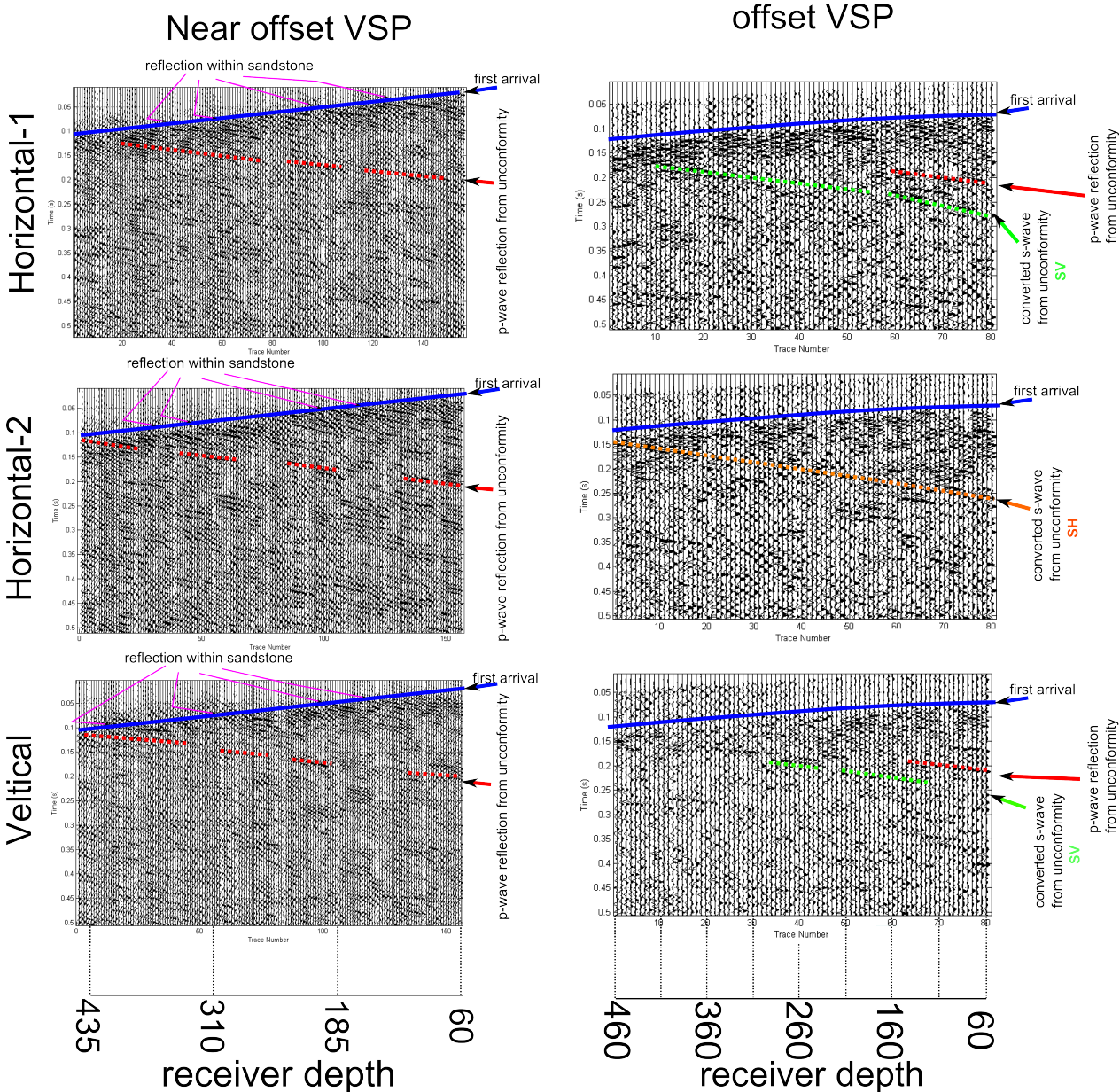
Figure 4.7: Processing results for the VSP surveys. The blue line labels the directed arrived p-waves. The red line labels the reflected p-wave events from the unconformity. The green and brown lines label the converted s-wave events from the unconformity, which can be only found on the offset VSP survey data. For the offset VSP survey, the rotation removed reflected p-wave energy completely from the Horizontal-2 component. The rotation does not separate p- and s-wave energy, as the polarization of neither p- nor s- wave is on the horizontal plan. Apparent p-p and p-s velocities are measured using the linear events. As source offsets of both surveys are small enough considering the survey depth, the apparent velocity of p-p and p-s event represents the p- and s- wave velocity of the Athabasca group sandstone.

rotated offset VSP data, the ground roll penetrates as deep as 100 m, resulting in the difficulty in measuring the shallow events. The p-wave velocity estimated by the first arrival is 2440 m/s. At the same depth, s-wave displays extreme low velocity of 300 m/s. As affected by the data quality, the up-going p- and s-wave events is not as distinguishable as the down-going events. The estimated up-going p-p and p-s event velocity agree with what suggested by the VSP processing report (Wolz & White, 2001). Both s-wave velocity ranges extracted from the VSP data and estimated from borehole logs are used in the modelling study in Chapter 5.

Chapter 5

Waveform simulations of the basement reflection

5.1 Elastic wave simulation
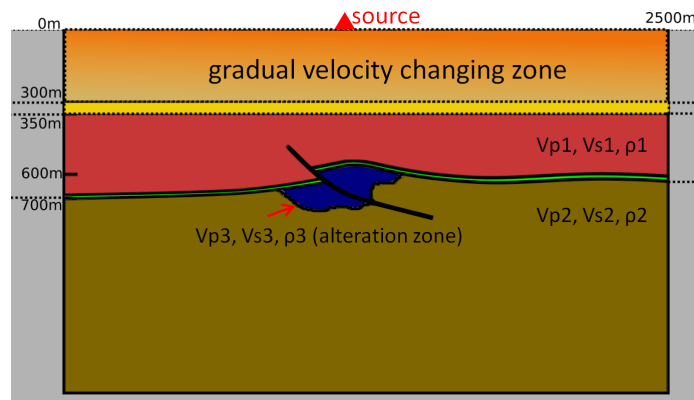
Figure 5.1: A sketch of geologic model considering multiple scenarios in Athabasca Basin, modified from Bolen, 2002). The Athabasca Group sandstone in the model consists of a gradual velocity changing zone overlying a thin layer within the sedimentary sequence. The Read Formation directly contacting basement rocks is set with a relatively high p-wave velocity, yielding a low velocity contrast with the underlying material. The blue area represents the altered mineralization zone, and the black line represents the fault zone (middle of the model). Seismic velocity and density are set differently within these units.

Methods described in Chapter 2 are commonly used in the oil and gas industries for AVO and reflectivity study, for targets depth are considerably deep. An assumption yielding the Zoeppritz equation includes the planar wavefront. Thus, the wavefield travelling directions are parallel with each other until encounter an interface. However, given a shallow target unconformity of a few hundred meters, the planar wavefront assumption can be invalid. The Zoeppritz equation may fail to accurately estimate seismic amplitudes in the Athabasca Basin, although it is calculated without any approximation methods. Numerical simulations of wavefields with spherical wavefronts are necessary for predicting amplitude behaviours quantitatively. For the simulation of wavefields, this study uses the software package SOFI2D

(Bohlen et. al., 2002), which is a finite difference (FD) seismic modelling tool. The algorism is based on the FD calculation of elastic wave equation. The method, as using the full elastic assumption, can predict the behavior of not only the reflected p-wave but also converted s-waves and surface waves. Kelly et al (1976) summarized the FD approach for creating synthetic seismograms, and the FD form of the elastic wave equation is the basis of SOFI2D algorithm. Two preliminary conditions are tested before numerical calculations. For avoiding grid dispersion, the grid spacing is limited:

$$dh \leqslant \frac{v_{s,min}}{n \cdot f_{max}} \tag{5.1}$$

where dh is the grid spacing, and $v_{s,min}$ is the minimum shear wave velocity specified in the model. f_{max} is the maximum frequency of the source wavelet. n is a parameter associated with the order of Holberg FD operator (Holberg, 1987). Courant et. al. (1928) denotes another condition for correcting and stable result from FD of partial differential equations that eliminate the time step used in the calculation:

$$dt \leqslant \frac{dh}{h\sqrt{2}v_{p,max}} \tag{5.2}$$

where dt is the time step. h, like n in the previous equation, is another parameter associated with the order of Holberg operator. $v_{p,max}$ is the maximum p-wave velocity used in the model.

For the simulation generated in this study, modellings are applied with the same absorbing boundary condition which is described by Cerjan et. al. (1985) to avoid reflections from the model boundary.

Parameters	Value	Parameters	Value
NProcX	2	Free Surface	at top
NProcY	2	Frame Width	50 m
FD order	8	Damping	6
NX	6000 m	Starting receiver	1750 m
NY	2500 m	Ending receiver	4250 m
dh	1 m	Sampling rate	0.5 ms
Total time	2 s	Receiver spacing	5 m
dt	0.05 ms	Samples per trace	4000
Number of time steps	40000	Number of traces	501
Source Type	Ricker, Explosive	File size	38.7 Mb
Source Frequency	50 Hz	Clock time for simulation	10000 s

Table 5.1: Parameters inputs for 2D finite difference modelling using SOFI2D software package

The 2D model for the numerical wavefield simulation is shown in Figure 5.1, the dimension is 2500 m wide and 1500 m deep. The Athabasca group sandstone in the model consists of three subunits: a gradual velocity increasing layer (above 300 m), a thin layer within the sedimentary sequence (300 m-350 m) and the high-velocity silicification zone in the sandstone (350-650 m). The p-wave velocity contrast along the unconformity is approximately 500 m/s. The fault and the altered mineralization zone are set with different s-wave velocities from the surrounding basement rocks. Receivers are placed on the surface from 0 to 2500 m to record the wavefield. Wavefield simulation and recording parameters are listed in Table 5.1.

NprocX and NprocY are numbers of processors on horizontal and vertical directions, respectively.
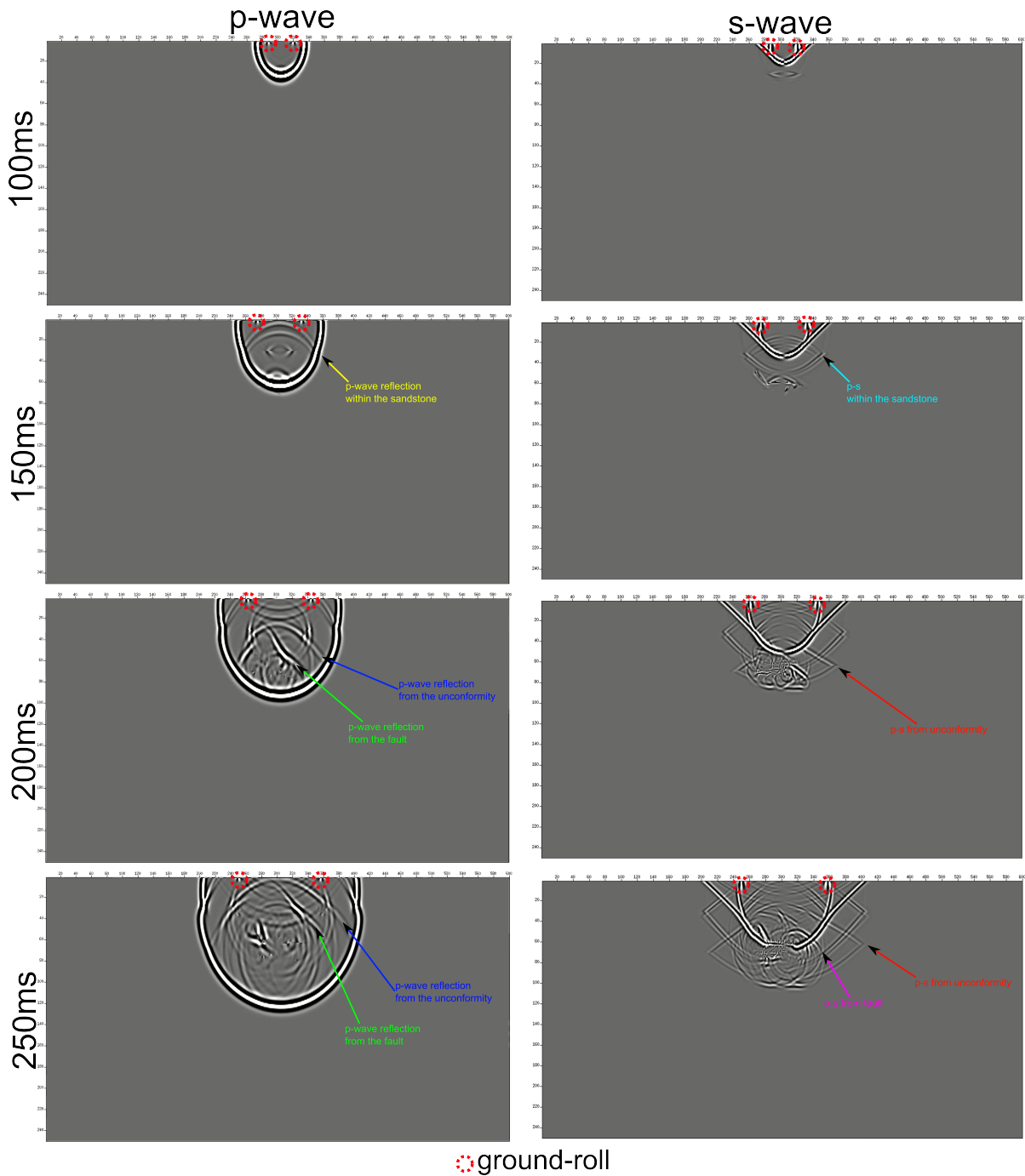
Figure 5.2: Snapshots of p- (left) and s- (right) wavefields during the simulation. Under the elastic assumption, surface wave travels with constant velocity and displays no frequency dispersion. Reflection of both p- and s-waves can be found within the sandstone, at the unconformity and from the fault. Converted p-s wave and s-p waves are also labelled.

For the simulation using a 4-core computer, the model is divided into 2*2 blocks for parallel calculations. The order of Holberg FD operation approximation can be 2, 4, 6, 8 and 12 for the SOFI software package. Higher order yields more accurate results but longer calculation time. The model dimension is enlarged on both sides and bottom for maximizing the avoidance of boundary reflection. Maximum grid spacing for avoiding dispersion is 4.336 m for the calculation, and 1 m is chosen. The maximum dt for stable condition is 0.0876 ms, so 0.05 ms is selected. The receivers are placed on the surface with total length of 2500 m, and they collect samples at every 10 time steps. The receiver spacing is 5 m yielding a 501 traces seismic record.

Figure 5.2 shows the snapshots of both p- and s-wave wavefields in the SOFI2D simulation. As the surface waves (ground-roll) contain both divergent and curl motions, they appear on both p- and s-wave snap shots and are distinguishable by relatively low apparent velocities. At an explosive Ricker wavelet source located at the surface, both p- and s- waves can be produced. As seen from the snapshots, the p-wave wavefront displays spherical characters with the depth of consideration. The s-wave wavefront has more planar forms. The changing of velocity from 300 to 350 m in the model produces significant p-p and p-s reflection at both the top and bottom boundaries, corresponding to the alteration conditions in the Athabasca group sandstone. The conversion of s-wave at normal incident angle is limited. Similar reflection and conversion occur when the p-wave wavefront encounters the unconformity, but as the physical properties within the fault is set differently from that of the surround, a clear p-p and p-s reflection can be also found on the snapshots.

A VSP survey can be modelled by the software package through placing the receiver line vertically. The receiver line has been located right below the seismic source at the center of the model (3000 m in x direction). The receiver spacing is 5 m with 78 traces, which covers the depth from 50 m to 435 m. The synthetic seismic record can be compared with the near offset VSP survey conducted in borehole MAC-218.

Figure 5.3 shows an example of the down-hole and surface recorded p-wave synthetic data. The record can be shown in either vertical and horizontal or s- and p- component. The zero offset time for p-p reflection from the unconformity is approximately 250 ms, and that for p-s converted wave is approximately 320 ms. The unconformity reflection can be distinguished from the p-p event produced by the thin layer within the Athabasca group sandstone. It tends to be overlapped by the s-p wave from that layer at far offsets because it is propagating with a similar apparent velocity. In contrast, up-going reflected, VSP recorded p-waves from the unconformity are clear from those interferences for two reasons. First, surface waves do not penetrate deep enough. Second, the s-p conversion is limited at the zero offset.
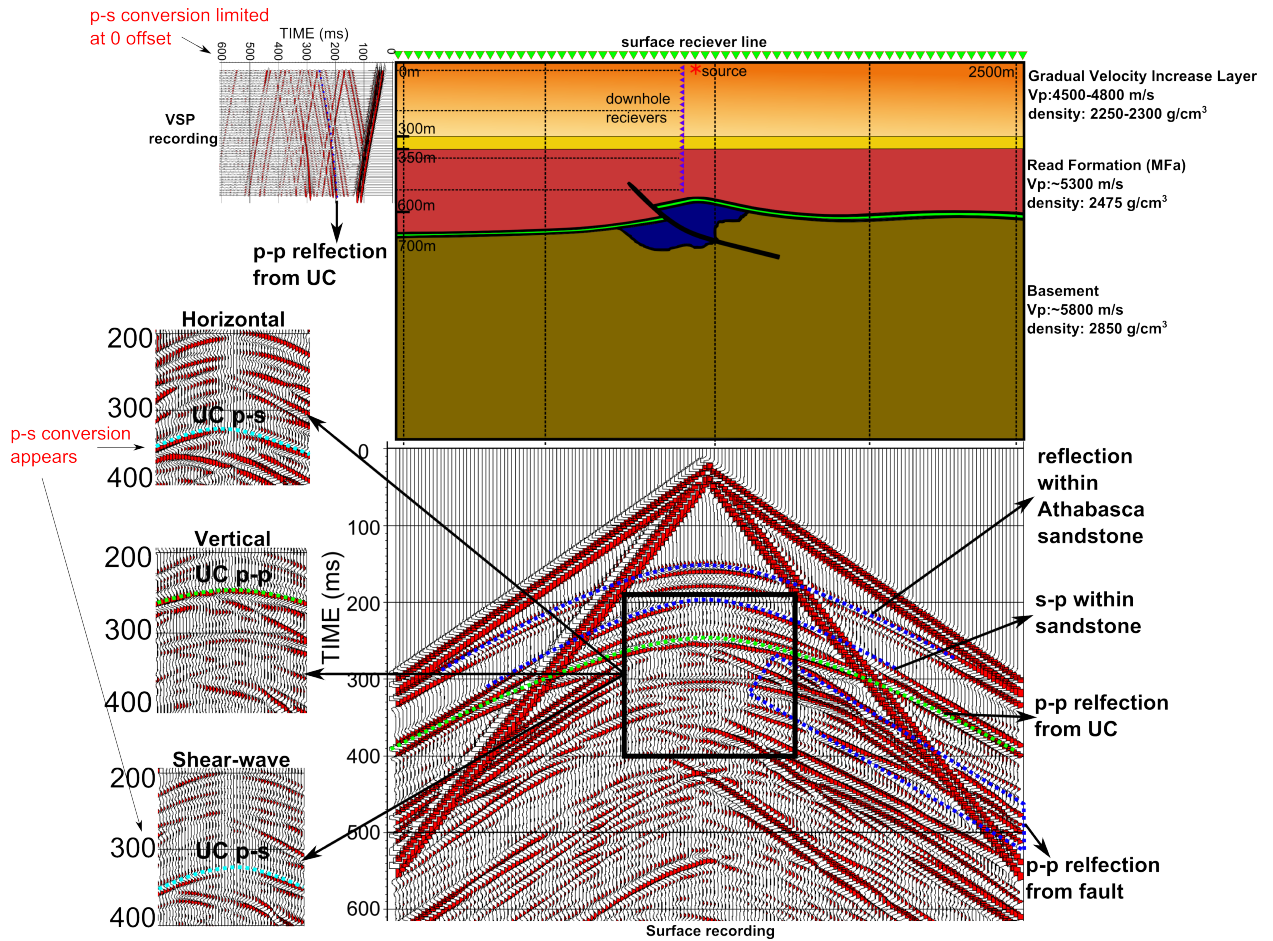
Figure 5.3: The model used for wavefield simulations (upper middle), the VSP recorded p-wave component of the elastic wavefield (upper left) and the surface recorded p-wave component of the elastic wavefield (bottom right). Major events are indicated on the surface record. UC stands for the basement unconformity. The bottom left three figures displays the horizontal, vertical and s-wave components of the recorded elastic wave field in the time window indicated in the p-wave component. The p-s wave from the unconformity is distinguishable on either the horizontal or the s-wave component record and arrives about 100 ms later than that of the p-p relfection.

5.2 Viscoelastic simulation

The viscoelastic model can be produced by introducing an absorption mechanism into the elastic simulation process (Bohlen, 2002). In SOFI2D, the mechanism of generalizing standard linear solid is applied. The absorption causes velocity dispersions and attenuations of the wavefield energy. The attenuation quality factor Q is defined by the reciprocal of seismic energy loss per cycle of oscillation over the total energy (i.e. E):

$$Q^{-1} = \frac{\Delta E}{2\pi E} \tag{5.3}$$

The velocity dispersion of body waves is conventionally neglected in seismic exploration because Q values for common geologic materials are large (>100); however, strong attenuations (low Q values) may enable measurements of dispersions. Liu et. al (1976) denotes that the frequency-dependent velocity relates with Q values:

$$\frac{V_{f_2}}{V_{f_1}} = 1 + \frac{1}{\pi Q} \ln \frac{f_2}{f_1} \tag{5.4}$$

where V_{f_1} and V_{f_2} are velocities for frequency f_1 and f_2, respectively. The equation provides theoretical basis for Q inversion (Sun et. al., 2009).

Figure 5.5 shows that p-wave first breaks of a near-offset field VSP survey (Chapter 4) and the synthetic VSP first breaks from the same model (Figure 5.1) with different Q values (6, 20 and 60). The apparent attenuation extent of the field VSP data tends to fall between Q=6 and Q=20 synthetic examples, suggesting an extremely low Q condition in the Athabasca Basin.

5.3 Summary

The 2D finite difference simulation of the seismic wavefield is generated by the software package SOFI2D with both elastic and viscoelastic assumptions. The elastic wave simulation suggests the existence of both p- and s-wave events. A reference shot gather of the 3C seismic data can be created by modelling through more detailed model parameters. The viscoelastic modelling suggests an extreme low Q condition compared with the field VSP data discussed in Chapter 4.

Multicomponent 2D and 3D seismic exploration survey has been conducted at the Athabasca Basin. The imaging of the basement unconformity and the alteration zone should be considered as difficult targets because of the possible low seismic p-wave reflectivity and strong attenuation conditions. The multiple information contained in the multicomponent 3D seismic data may allow further detailed mapping of where the reflected p-wave imaging fails. In the low p-wave impedance contrast region, the analysis or inversion of amplitude derived attributes (e.g. Poisson's ratio) could be useful for the detection of alteration zones. In addition, s-waves could joint with p-waves to image the unconformity because of a different AVO behaviour. The strong attenuation condition lowers the signal-to-noise ratio of the original field record, but may cause measurable body wave dispersion, which will allow the analysis of Q factors providing new potential attribute anomalies for inversion. The modelling study will be used to guide processing of multicomponent converted s-waves of the seismic data at the Athabasca Basin. S-wave velocity measurements in the future may offer better results for both modelling and inversion procedures.
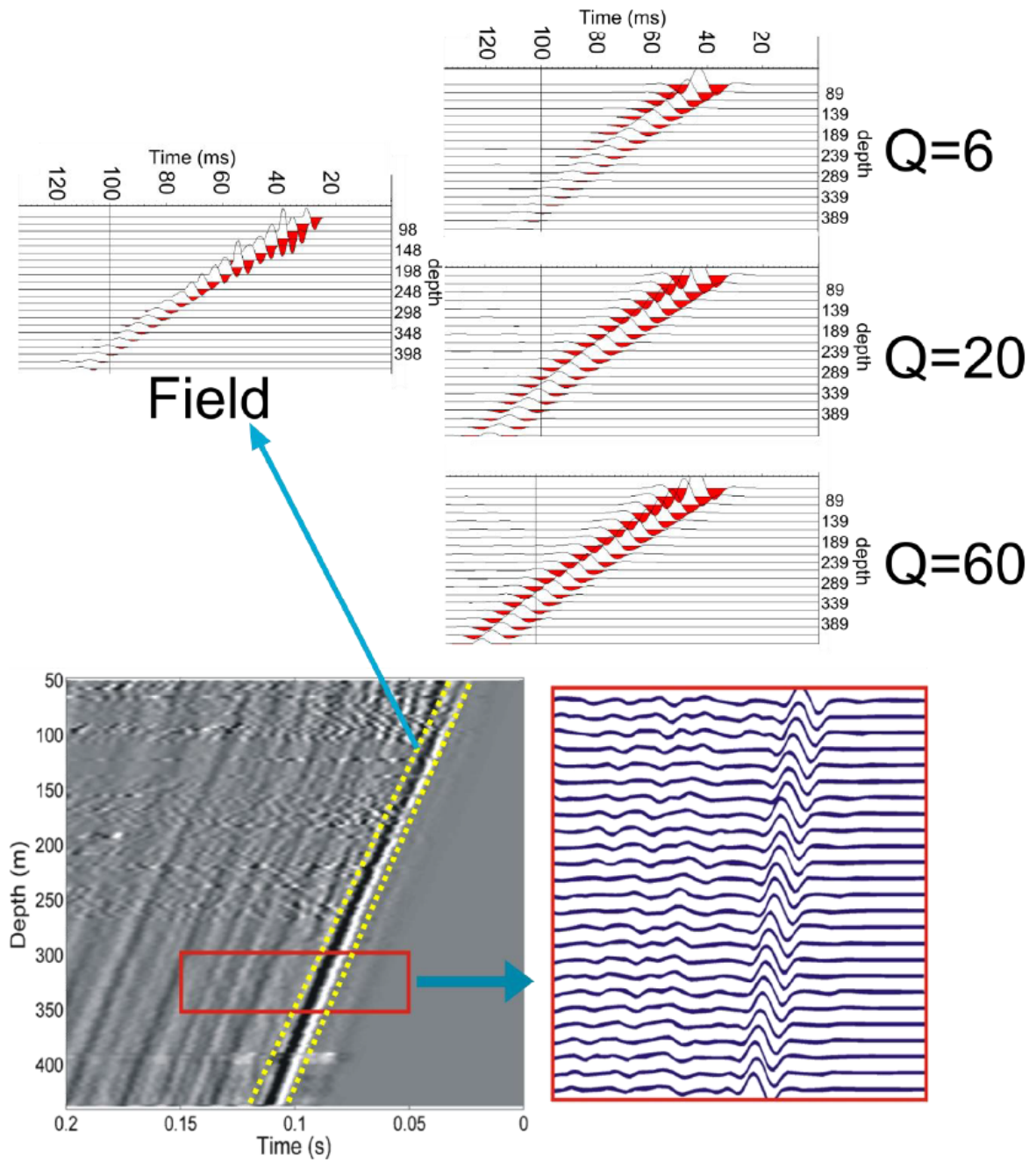
Figure 5.4: Comparisons of p-wave first breaks of simulated VSP surveys with different Q values (upper right) and the field VSP record (upper left) from a borehole in McArthur River. The upper left example is extracted from the raw VSP data (lower left) using a sparse geophone spacing. The lower right figure is a zoom-in of the raw data to view the shape of first breaks. (Sun et. al., 2013)

Chapter 6

Summary

The seismic exploration methods used nowadays are developed from the oil and gas industry, focusing on deep targets (mostly >2 km) in a sedimentary environment. For a shallow detection of mineralization in hardrocks, like seismic exploration projection in the Athabasca Basin, the commonly used strategies fail or face difficulties. In the Athabasca Basin, seismic work aims to map the basement unconformity and, expectantly, image the mineralization zones. Alteration conditions control the p-wave reflectivity along the unconformity. Silicification alteration in the Athabasca group sandstone can potentially increase the p-wave velocity, while argillic alteration will decrease the velocity. Where p-wave velocity contrast is small, low reflectivity occurs. The condition tends to be severer near the uranium mineralization, as the formation of which is associated with the alteration.

Considering conventional seismic exploration using reflected p-waves, the signal from a target interface is enhanced by the common-midpoint stacking process. The process neglects the incident-angle dependent reflectivity. Amplitude versus offset effect is commonly occurred in many geological settings. As long as the AVO behaviour of the target does not result in a phase turning, CMP stacking will still be an effective way to enhance the signal, and low reflectivity problem can be solved by simply acquiring seismic data with higher fold coverage. The calculation of AVO response using rock physical properties in the Athabasca Basin suggests that p-wave reflectivity does have great potential to change phases, and the stacking process in this situation will only result in suppression of the signal.

This does not result in a conclusion that p-wave is useless for the seismic exploration in the Athabasca Basin. Various technologies on AVO analysis is growing mature in the oil and gas industry. Most of them treat AVO behaviour as a distinct lithological indicator and produce images through attribute analysis or inversion. The AVO technologies from the oil and gas industry are predominantly focusing on fluid detection in porous media. Thus, the petrophysical study, which the AVO analysis is based on, is only available for sedimentary rocks with changing fluid types. For the seismic exploration in the Athabasca Basin, the fully brine saturated hardrock is completely different from what hosts the oil and gas. Even if AVO anomalies are observed in the seismic data, it is not related to the geology since rock physical properties are not well established. Besides the AVO analysis, the lack of petrophysical data causes difficulties for any future seismic work in the Athabasca Basin including 3D and s-wave processing.

S-wave can be another solution to the p-wave imaging problem. The 3D 3C survey generated in Millennium area has great potential for s-wave analysis. Unlike p-wave, s-wave AVO responses never show a phase turning. The reflectivity of converted s-waves is limited at near offsets, which requires a

large maximum offset in the seismic acquisition. The processing of s-wave data requires s-wave velocity information, which has not been measured in boreholes in the Athabasca Basin. This research proposes an approach to estimate s-wave velocity using borehole geophysical measurements based on the effective media assumptions. There is no data to confirm the accuracy of the estimation, so it can be tentatively used in the s-wave processing and modelling study. With detailed inspection in the VSP survey conducted in borehole MAC-218, s-wave existence is confirmed. The inspection also denotes that in order to better achieve processing results, a complete separation of p- and s-wave wavefields involving 3D rotation should be implemented for the 3-component data. The Appendix in the report proposes a new method to separate p- and s-wave energy on a seismic section based on the reverse and forward extrapolation of the wavefield.

Considering a deep exploration target, the AVO calculation for both p- and s-waves can be generated quantitatively and accurately by solving the Zoeppritz equation. The planar wavefront assumption for deriving the Zoeppritz equation can be invalid for the shallow target unconformity in the Athabasca Basin. The full elastic 2D finite difference modelling of the seismic wavefield can be used to predict the p- and s-wave behaviours for the uranium exploration in the Athabasca Basin. With larger and more accurate data based on the petrophysical properties, the synthetic data acquired from the input geological model can be used as a reference for all components of the surface recorded with elastic events (p-, s- and surface waves). In the Athabasca Basin, the significant near surface absorbing condition controls the signal to noise ratio of the seismic data, which cannot be predicted by reflectivity. The viscoelastic modelling generated using the SOFI2D software package denotes that the Q value near borehole MAC-218, where the VSP survey is conducted, is between 6 and 20, which is much smaller than the conventional seismic exploration in sedimentary environment. Thus, the parameter for Q compensation and surface consistency process can be essential for a good seismic data quality. Moreover, the strong attenuation condition may yield measurable velocity dispersion of p-wave first arrivals, and Q value can be developed as another seismic attribute for inversion.

Analyses of p- and s-wave data can derive different seismic attributes (p-wave velocity, s-wave velocity, Poisson's ratio etc.). A sophisticated method of integrating different types of rock physical properties is required for the inversion of multi-attribute data. The reverse-time migration, which is equivalent to a full-waveform inversion process, can be tested using different physical models. An acoustic example of borehole seismic data is given by this study, which denotes that the seismic data acquired in the borehole as a VSP survey can be potentially useful for imaging the unconformity in the Athabasca Basin.

Appendix A

Reverse-time migration for borehole seismic data

Considering the exploration of shallow targets, like uranium seismic project in the Athabasca Basin, the reflection survey can be significantly affected by the near-surface conditions. The ground-roll smears reflection event, and the loosely packed overburden yields very strong attenuation conditions. This gives advantages of borehole seismic data to image the unconformity, or better assists surface seismic analyses. Few limitations of pre-stack reverse-time depth migration on reflector dipping angle or source-receiver geometry make itself a suitable tool for migration of borehole seismic data. The appendix discusses a test on reverse-time migration based on finite difference (FD) solution of 2D wave equation in applying on synthetic borehole seismic data generated by different geologic models. The generation of synthetic borehole seismic data was conducted by solving 2D acoustic and elastic wave equations. The synthetic seismogram of acoustic modelling contains p-wave only, and that of elastic modelling is a full-waveform record with the presence of both p- and s- waves and surface waves. Acoustic wave equation is used for extrapolating the recorded wavefield backwards, and different behaviours of events other than primary reflected p-waves are examined.

Various approaches for migration of recorded seismic wavefield (vs. time) using finite-difference algorithm have been studied since the 1970s. Claercout (1985) summarized the conventional FD migration methods based on downward (i.e. direction of depth) extrapolation of stacked zero offset surface wavefield record. McMechan (1983) and Baysal (1983) introduced a migration process by extrapolate the recorded wavefield backwards with time using FD solution of 2D acoustic wave equation for synthetic surface zero-offset seismic data. This process is known as reverse-time migration (RTM). Because the algorithm includes paraxial terms that have been approximated during conventional FD migration algorithms, the reverse-time extrapolation is able to accurately locate even 90° dipping reflectors. The full-waveform character of RTM enables preservation of real amplitude of multiple events (i.e. p-p, p-s etc.) during migration processes of pre-stack common shot gather, if appropriate imaging condition and elastic wave equations are implemented.

Borehole seismic record (i.e. VSP) has a form of shot gather, and 3-component VSP survey is common nowadays. Conventional imaging of VSP record involves VSP-CDP conversion, which is not suitable for dipping reflector and intense lateral velocity variation model. Keho (1984) and Wiggins (1984) introduced Kirchhoff migration into VSP data imaging process, which has become a commonly

used VSP migration technique. Kirchhoff migration is not applicable to be implemented in the area with complex subsurface geology because it is sensitive to large lateral velocity variation. Using the time-coincidence imaging condition described by Claerbout (1971) and the same as that used in Kirchhoff VSP migration by Wiggins (1984), Sun and McMechan (1986) and Chang and McMechan (1986) tested pre-stack reverse-time migration of synthetic offset VSP data by FD solution of 2D elastic wave equation. The results imply a different resolvability of vertical and horizontal receiver components on horizontal and vertical geologic features. Sun and McMechan (1986) denoted a potential limitation of FD algorithm on randomly spaced VSP data, so Chen (1987) studied both surface and VSP reverse-time migration by finite element scheme of 2D acoustic wave equation. Chen and McMechan (1992) applied acoustic reverse-time migration for both synthetic and real 3D VSP data, bringing the technique into 3D areas. Hokstad (1998) implemented 2D elastic reverse-time migration on a real marine walk-away VSP data acquired offshore Norway.

For the acoustic testing, both forward modelling and RTM algorithm are based on the 2D scalar acoustic wave equation:

$$\frac{\partial^2 P}{\partial x^2} + \frac{\partial^2 P}{\partial z^2} - \frac{1}{v_p^2(x,z)}\frac{\partial^2 P}{\partial t^2} = 0 \tag{A.1}$$

where P(x, z, t) is the p-wave wavefield corresponding to the displacement of particles along p-wave propagation direction, x is the horizontal axis, z is the vertical axis (positive downward), t is time axis and v_p is p-wave velocity (Courant and Hilbert, 1962). The FD form of the acoustic wave equation is given by McMechan (1983, one printing error of the equation was on the original paper):

$$U(x_k, z_j, t_i) = 2(1 - 2A^2)U(x_k, z_j, t_{i-1}) - U(x_k, z_j, t_{i-2}) +$$
$$A^2[U(x_{k+1}, z_j, t_{i-1}) + U(x_{k-1}, z_j, t_{i-1}) + \tag{A.2}$$
$$U(x_k, z_{j+1}, t_{i-1}) + U(x_k, z_{j-1}, t_{i-1})]$$

where $A = v_{p(x=k,z=j)}\Delta t/h$, Δt is the time step between two successive wavefields ($\Delta t = t_i - t_{i-1}$), and h is the length between two grid points. This is the FD equation of 2D acoustic wavefield forward modelling. The condition for local stability is:

$$\Delta t < \frac{h}{v_p\sqrt{2}} \tag{A.3}$$

The wavefield at one time step (i.e. $U(*, *, t_i)$) is able to be determined by the wavefield at the time step before (i.e. $U(*, *, t_{i-1})$) and that at two time steps before (i.e. $U(*, *, t_{i-2})$). At one specific point, $U(x_k, z_j, t_i)$ is given by both the temporal terms:

$$2(1 - 2A^2)U(x_k, z_j, t_{i-1}) - U(x_k, z_j, t_{i-2}) \tag{A.4}$$

which only involves wavefield information at that point, and the spatial term:

$$A^2[U(x_{k+1}, z_j, t_{i-1}) + U(x_{k-1}, z_j, t_{i-1}) + U(x_k, z_{j+1}, t_{i-1}) + U(x_k, z_{j-1}, t_{i-1})] \tag{A.5}$$

which only involves wavefield information at the time step before (i.e. $U(*, *, t_{i-1})$). That enables the FD operation to march either positive or negative direction with time. If switch $U(*, *, t_i)$ and $U(*, *, t_{i-2})$ terms and change notation on i, we get:

$$U(x_k, z_j, t_i) = 2(1 - 2A^2)U(x_k, z_j, t_{i+1}) - U(x_k, z_j, t_{i+2}) +$$
$$A^2[U(x_{k+1}, z_j, t_{i+1}) + U(x_{k-1}, z_j, t_{i+1}) + \tag{A.6}$$
$$U(x_k, z_{j+1}, t_{i+1}) + U(x_k, z_{j-1}, t_{i+1})]$$

this is the FD equation of 2D acoustic wavefield for reverse-time migration. The concept is illustrated by Figure A.1.
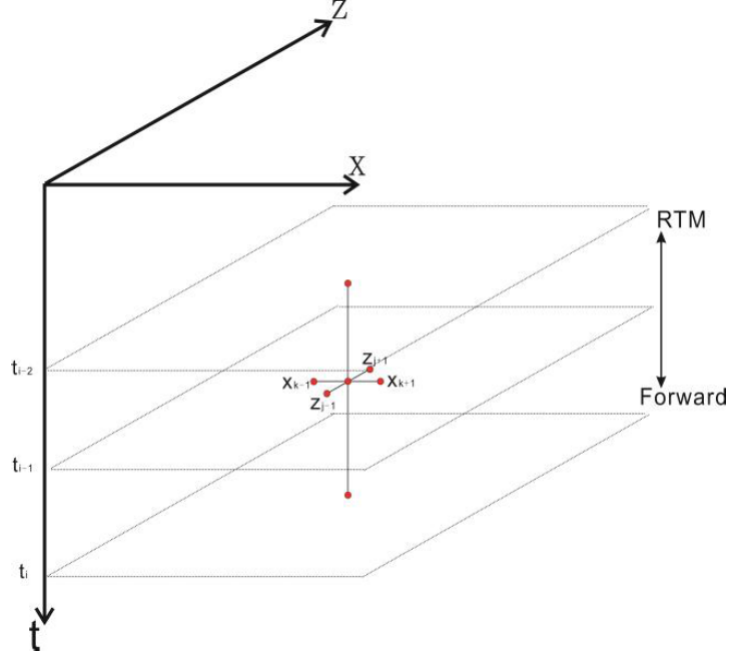
Figure A.1: Illustration of finite difference operation of 2D scalar wave equation at a given grid point. Forward modelling marches the wavefield to time positive infinite, while RTM algorithm is on the opposite direction

A set of MATLAB codes for generating the acoustic model and running acoustic wavefield extrapolation are conducted.

Figure A.2 shows the models used for the generation of synthetic seismic data. Arbitrary source-receiver geometry can occur in borehole seismic surveys. For instance, receivers locate in a vertical or horizontal well with either near or far offset. Three models with receiver located in both vertical and horizontal well are used to generate the synthetic seismic data in for forward problem. For the acoustic testing, the model will only involve changes of p-wave velocity. Models are created in the same dimension of 400*700 grids. The distance between each grid is 10 m. Starts from 100 grid points away from the model edges, except the surface, is where the absorbing boundary condition (Cerjan et. al., 1985) is applied. Surface of each model is defined by the p-wave velocity of air (i.e. 340 m/s). The single source is located at the center of the calculation model (i.e. without absorbing boundary at x=3500 m, y=1500 m). Instead of a point source, a Gaussian shaped function is defined for easier calculation of initial conditions.

As mentioned in Chapter 5, the stable condition denotes a maximum time step of 2.357 ms for a simulation without grid dispersion. The time step used in the calculation dt is 1 ms, and total time for the simulation is 2500 ms. Results of simulation suggest the total simulating time being unnecessarily
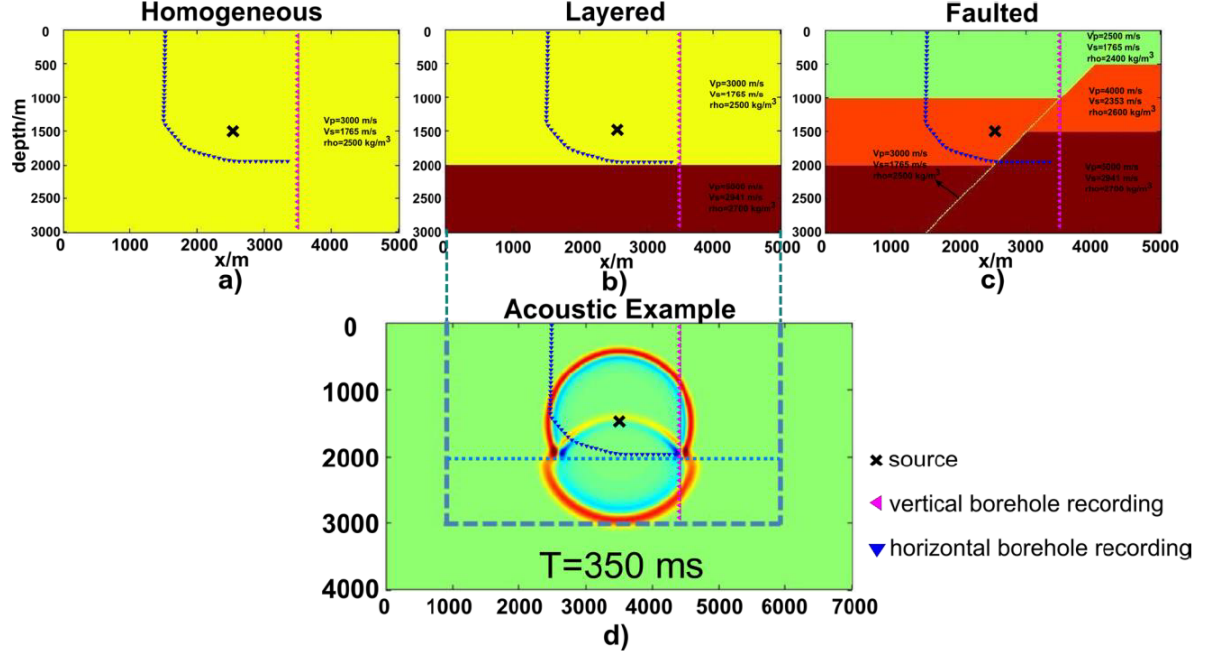
Figure A.2: Three models created for generation of synthetic seismograms in the forward modelling. a) Homogeneous model b) Layered model c) Faulted model. The simulation of wavefield is recorded by both a vertical and horizontal borehole receiver layout. d) a snapshot of the acoustic wave field for the layered model at 350 ms

large.

The forward model simulation applied a nonreflecting boundary condition described by Cerjan (1985). Amplitude of wavefield propagating in the absorbing frame is multiplied by a G factor:

$$G = e^{-[a(bl-i)]^2} \tag{A.7}$$

where i is a counting index start from i=1 at the edge of entire model to i=100 at the inner side of the model. bl is the width of boundary. a is defined by the following equation:

$$a = \sqrt{\frac{-\ln(1-Q)}{bl-1}} \tag{A.8}$$

where Q defined in parameter file (i.e. 97% in this research) is the percentage of amplitude absorption (i.e. 1-G) at the edge of the boundary. Thus, a gently decreasing G (i.e. from 100% to 3% in this case) absorbs the amplitude of wavefield propagating in the boundary with respect of grid points. As no absorption is applied at the inner part of the boundary frame, no reflection could occur at the boundary if parameters (i.e. bl and Q) are well determined.

The program defines the position of receivers by applying an R matrix of the same size of the model, which enables the possibility of implementation of receivers anywhere in the model. The matrix is assigned to 1 at one receiver position and 0 at the other. The receiver spacing is 1 grid point (10 m). Receivers take records of local wavefield at each time step (i.e. thus sampling rate=1 ms) and then organized by the order from left to right and from top to bottom to create seismograms. Thus the x axis of a seismogram only represents the trace number instead of the real positions of the receivers.

47

Figure A.3: Examples of vertical and horizontal recorded seismograms for each of the model during acoustic simulation. Simulating time is 2.5 s, and the receiver spacing is 10 m on straight sections of the recording line

The definition of initial condition (i.e. define $U(*, *, t_{i-1})$ and $U(*, *, t_{i-2})$) is based on the Gaussian function. The Gaussian function curve centred at x=0 and with =45 (user defined) is rotated to form the initial displacement of the wave field. Olver (2013) composed a detailed introduction on the calculation of initial conditions of wave equation, in which the wavefield at the next time step ($U(*, *, t_{i-1})$) can be created by:

$$U(r_{x,z}, t_{i-1}) = U(r_{x,z}, t_{i-2}) + \frac{\partial U(r_{x,z}, t_{i-2})}{\partial r} \mathrm{d}t + \frac{V^2(x, z)}{\mathrm{d}t^2} \frac{\partial^2 U(r_{x,z}, t_{i-2})}{\partial r^2} \tag{A.9}$$

as here Gaussian function is rotated with respect to source position. Derivative on radius (i.e. r in equation above) direction of wavefield in the polar coordinate centred at source position gives the local gradient of the wavefield.

For RTM, each receiver is considered to be a local source that is reverse-time vibrating of its own recording (i.e. starting from 2500 ms in this example), which contributes to the initial condition of the RTM calculation. The wavefield is propagating to every direction locally instead of only propagating to the source position, which will result in propagation of half of the total energy in the opposite direction with respect to the source position. It occurs as a major problem especially when dealing with VSP and horizontal well simulations. To avoid this situation, either a one-way finite differentiate wave equation can be used or a non-vibrating boundary can be implemented beside the receiver on the opposite direction to the source. The study used the second one by returning zero of the wavefield beside receiver location.

Using the same geological model (Figure A.2) and acquisition parameters, the forward modelling for generating elastic borehole seismic data is done by SOFI2D (Bohlen, 2002). The reverse-time migration process is conducted by the algorithm with the acoustic assumption.
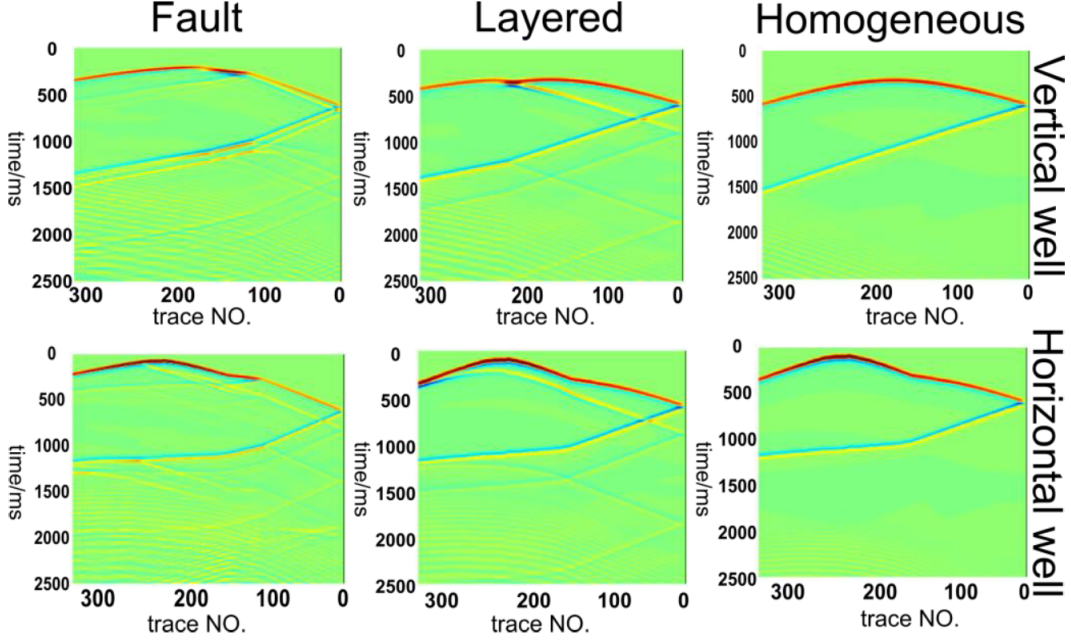
Figure A.3 shows an example of vertical and horizontal recorded seismogram for each of the model

during the acoustic simulation. The simulating time is 2.5 s, and the receiver spacing is 10 m on straight sections of the recording line. For each of the modelling, direct arrived and surface reflected wavefield energy accounts for more than 80% of the recorded total energy. The reflected event in the layered model shows in-phase character with the direct arrival, while the reflection from the surface displays opposite phase. In the fault model, source energy tends to be trapped in the layer from 1000 to 2000 m depth, which has been well recorded in the horizontal well.

Figure A.4 shows the snapshots of reverse-time extrapolation of the wavefield recorded by vertical and horizontal wells for the layered model. Both wavefields are mostly correctly reversed to the source location. The ends of the receiver lines are tend to perform as point sources propagating to every direction during the RTM process, which results in the diffracting event at the t=0 section.
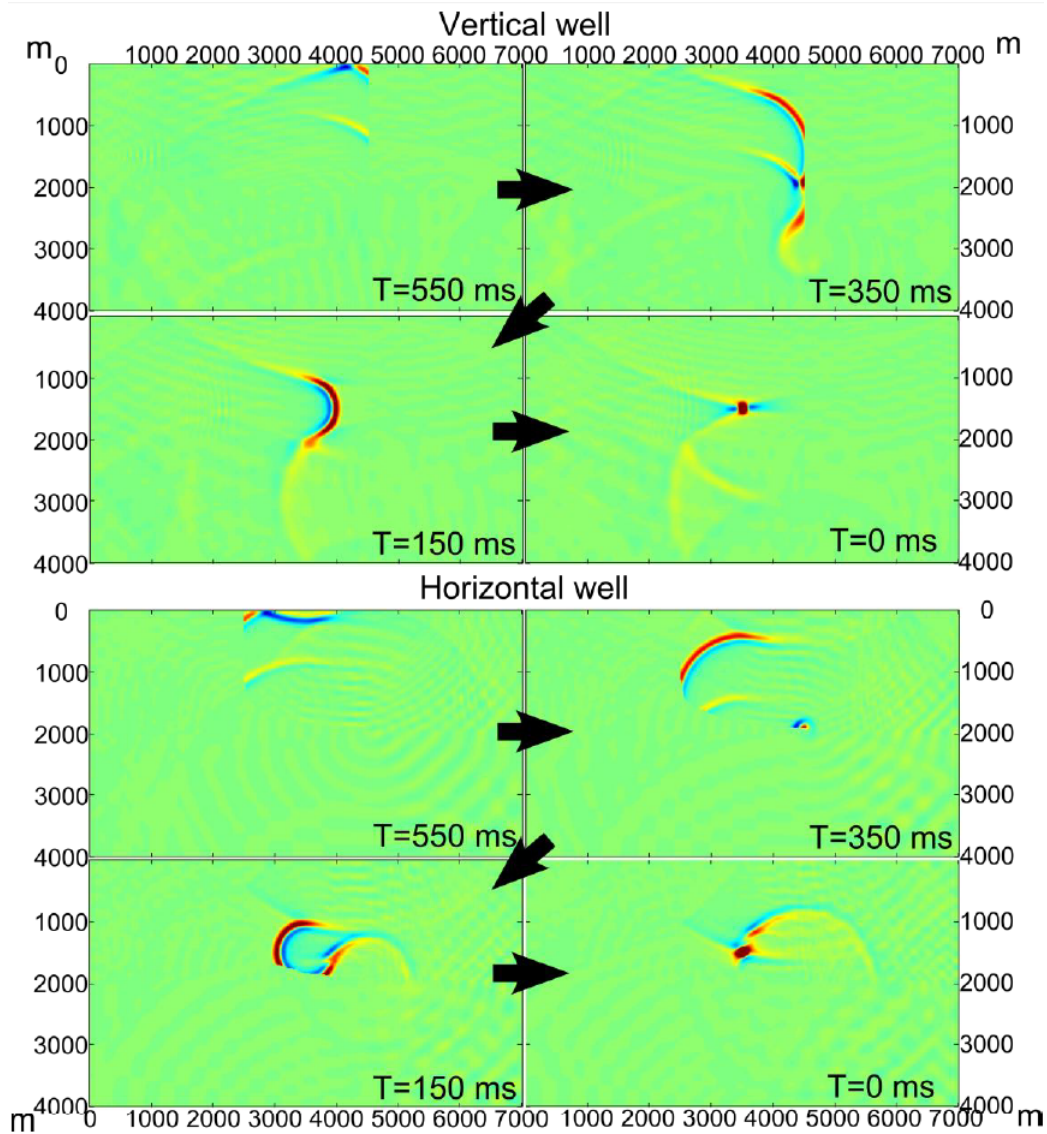

Figure A.4: Snapshots of reverse-time extrapolation of the wavefield recorded by vertical and horizontal well for the layered model.

Figure A.5a shows the horizontal component of the synthetic data produced based on elastic wave

equation for the layered model recorded by the vertical borehole receivers, and Figure A.5b displays the snapshots of reverse-time migration of that record. The seismogram contains both p- and s- wave events. Both transmitted and reflected s-waves appear on the horizontal component of the seismogram. On the snapshots of RTM, converted p-s wave from the surface and transmitted p-s wave are distinguishable until 400 ms. The converted p-s wave from the interfaces shows a divergent character that disappears on the snapshots as a result of spherical spreading.

As RTM is mostly considered as a pre-stack migration process, the s-wave energy in the data is still well preserved, which will cause noise if acoustic RTM is applied. There are two types of methods to solve the problem: either by separating the p- and s-wave energy on the pre-stacked data (described in the Chapter 4), or by applying elastic wave equation during the RTM process.

As seen from the RTM results, when considering only the p-wave for the recorded acoustic wavefield, source location can be well located even when the model shows strong heterogeneity. An apparent advantage of the RTM applied on the borehole seismic data is the absence of surface waves. The image of RTM with arbitrary source-receiver geometries can be greatly affected by the heterogeneity of the geological model, for the elastic case, even the velocity model is known. The s-wave energy component in the elastic wavefield cannot be located correctly using acoustic wave equation. This suggests a separation of s- and p-wave wavefield energy before the RTM for the down hole seismic data, or even an application of the elastic equation.

To generate an effective reverse-time migration process for seismic data, two preconditions are required: first, the imaging condition used, and second, the wave equation for the algorithm. The modelling is conducted with receiver located in the center of the model, which is an equivalence of the exploding reflector imaging condition. The condition assumes the zero-offset seismic section is equivalent to the double time section of placing sources on the subsurface reflector (Claerbout, 1971). It is commonly used in a conventional post-stack migration process. In the modelling study, the direct arrived p-wave can be seen as one of the imaging points of the reflector. Thus, the interface in the one-layer model is actually the second interface on a true seismic section. Seen from the modelling results, only the direct arrived p-wave field can be reversed to the correct location, and reflection from a second interface will result in noisy events in the reversed section. To avoid the noisy problem from a second interface during the RTM process, the cross-correlation imaging condition should be applied. However, it is not tested in the modelling study. The modelling described in the report uses both acoustic and elastic wave equations for producing synthetic seismic sections, but the reverse-time migration process is only tested using the acoustic assumption. The consequence, as seen from the reversed result sections, indicates that s-wave wavefield cannot be reversed to the source location, as it is not predicted by the acoustic wave equation. In conclusion, for the RTM imaging of a reflector using both p- and s-wave field energy, elastic assumption and cross-correlation (or more sophisticated ones) must be applied to the algorithm. Thus, the modelling study is an imperfect example of the RTM process considering imaging the unconformity.

The acoustic reversing of elastic seismic data set has potential usage in other aspects of processing rather than migration. As described in Chapter 4, the complete separation of p- and s-wave wavefield involves the determination of target reflected p-wave event polarization, which is not easy to achieve if the signal to noise ratio is low. The situation is common for the surface seismic survey when p-wave reflection interferes strongly with surface and multiple waves as seen in Figure 1.5. The separation of p- and s-wave wavefields can be achieved by a new concept based on RTM algorithm without determining the polarization.
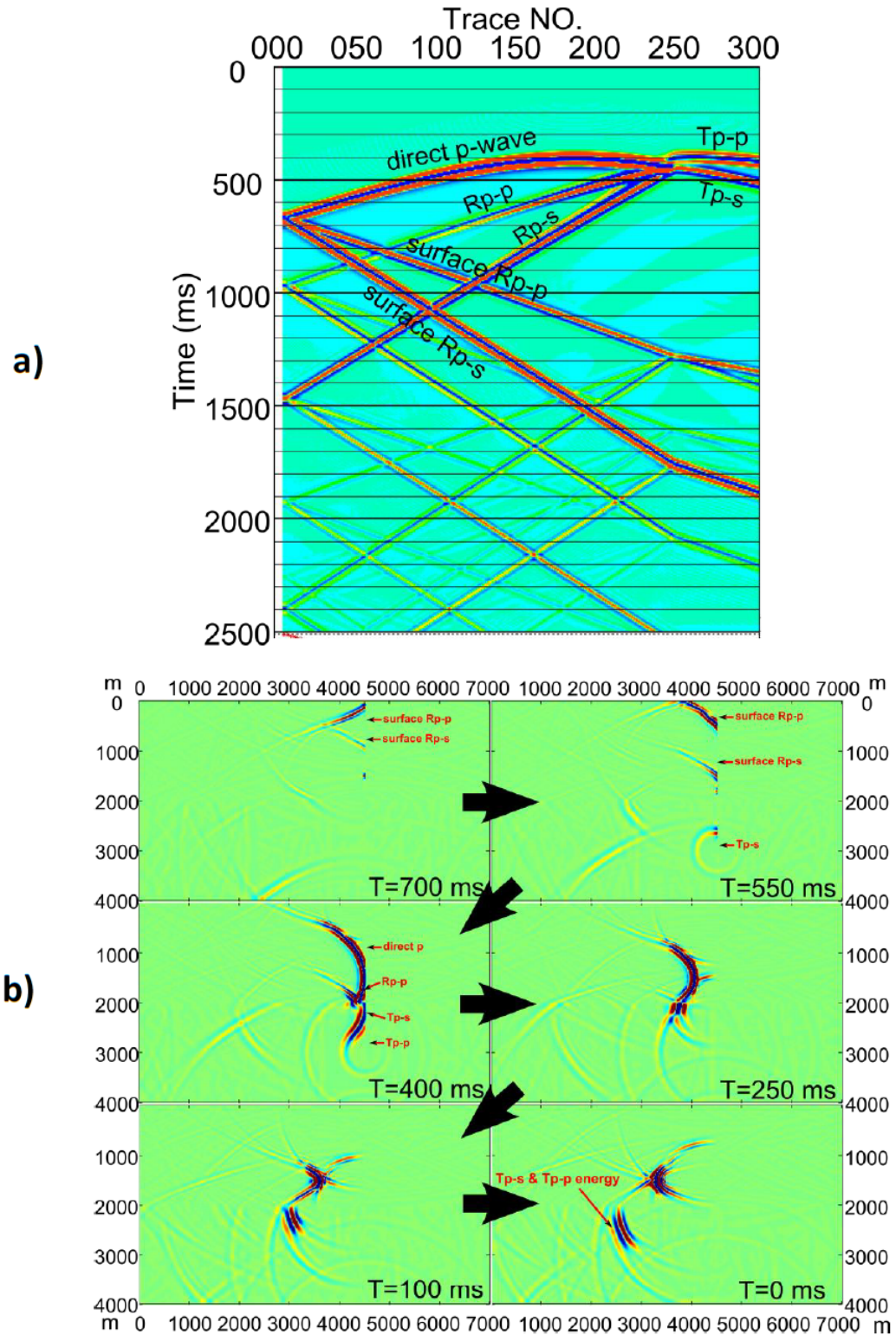
Figure A.5: a) the horizontal component of the synthetic data produced based on elastic wave equation for the layered model recorded by the vertical borehole receivers. The seismogram contains both p- and s-wave events. b) Snapshots of reverse-time extrapolation of the vertically recorded elastic wavefield shown in Figure 4. S-wave energy ends up to incorrect location at finishing time.
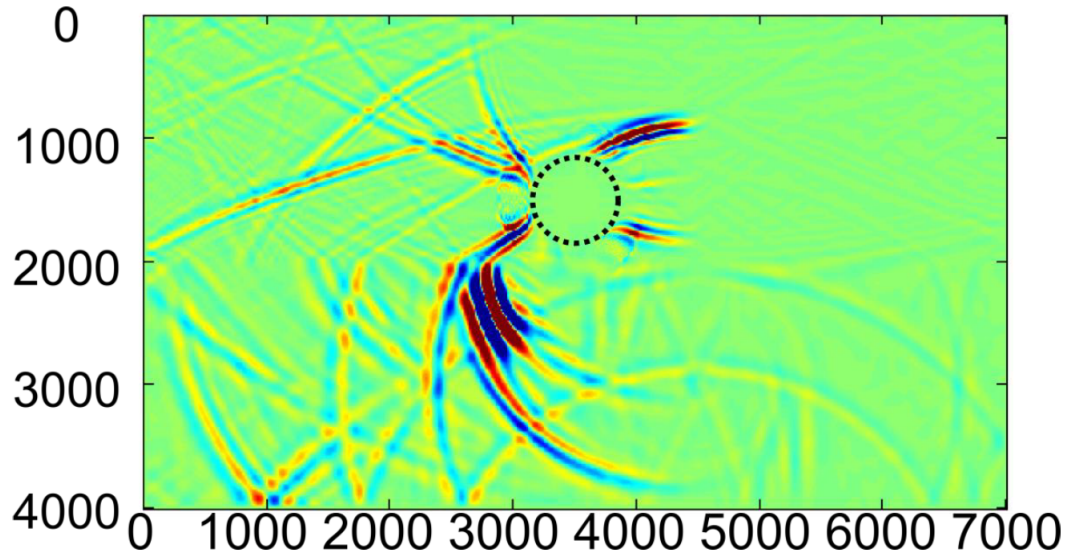
51

Figure A.6: Reversed wavefield snapshot at T=0 ms with p-wave energy at source location wiped out. The real source location is at x=3500 m, y=1500 m of the model. Wavefield within radius of 500m from the source location is set to 0. The wavefield without p-wave energy is extrapolated forward to reproduce the seismic trace without p-wave energy.

Because the extrapolation of wavefield is a reversible process, the reverse-time extrapolated wavefield can be reproduced using the same algorithm. By reverse-time extrapolation of the elastic wavefield seismic record using acoustic wave equation, only p-wave is correctly propagated to the source location (the example from Figure A.5). By knowing the source location in the model, p-wave energy can be wiped out from the reversed wavefield. By the forward propagation applying the same acoustic algorithm, the wavefield without p-wave energy can be extrapolated forward to reproduce the seismic trace with only s-waves.

One example of the wavefield used for forward extrapolation is given in Figure A.6. The correctly reversed p-wave energy within 500 m from the real source location is wiped out (set to 0). The reproduced seismic section is shown by Figure A.7. The imaging condition used by the algorithm can only correctly reverse the direct arrived p-wave energy and the p-wave reflected by the surface. These events are successfully removed from the seismic section. Compared the reflected p-wave from the surface (Figure A.4), the converted s-wave from the surface is preserved well. As partial missing of the energy, converted s-wave from the surface is not strictly travelling with the correct velocity. Reflected p-wave, transmitted p- and s-waves from the interface are reproduced in the reversed section. The converted s-wave from the interface is lost, because the energy is reversed to the area within 500 m of the source location. Generally, the p-wave energy of the major events can be removed using this method without hurting most of the s-wave events.
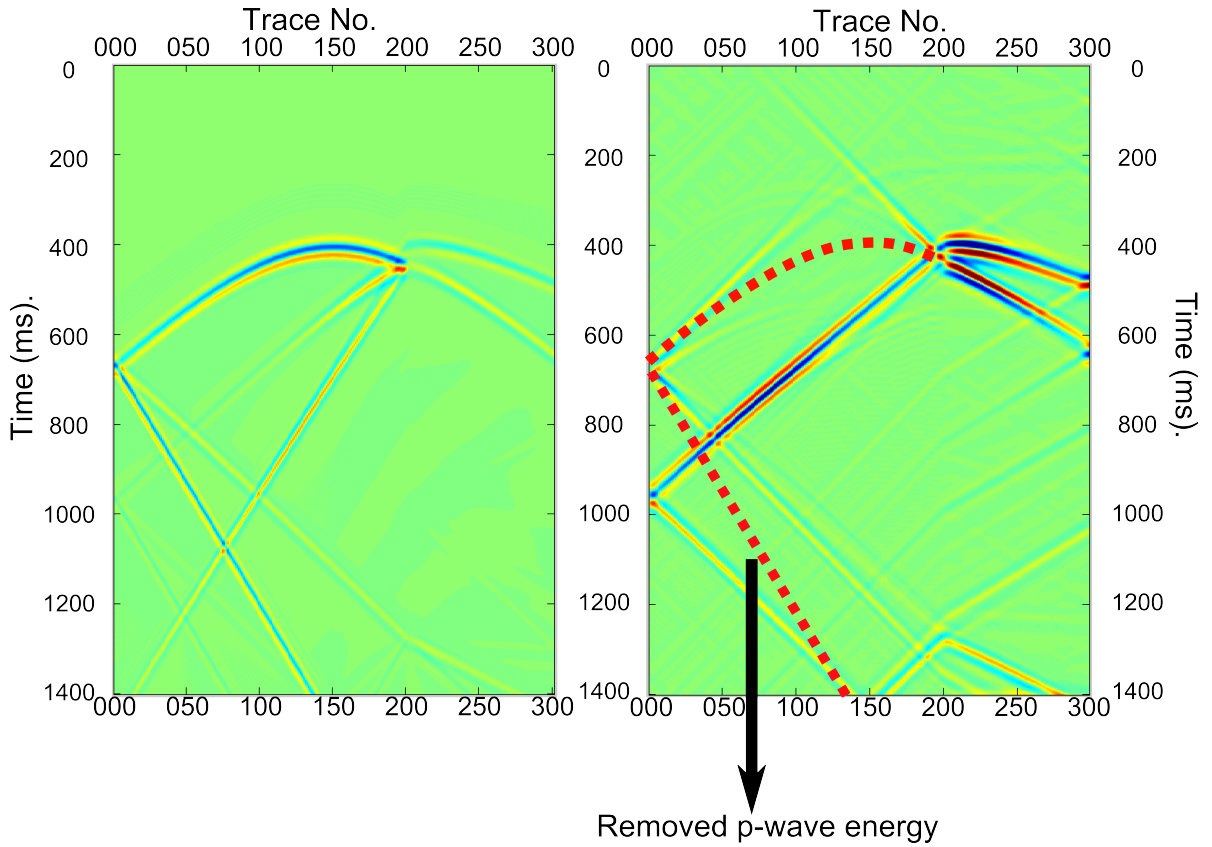
Figure A.7: The comparison of original time section (left) and the reproduced time section with p-wave energy wiped out (right). The red dashed lines represent removed p-wave energy by the process. The curved part of the dashed line is the directed arrived p-wave energy, and the straight part of the line is the reflected p-wave energy from the surface.

Bibliography

Balch, A. H., and Lee, M. W., Eds., 1984, Verticalseismie profiling:Techniques, applications, and case histories: International Human ResourcesDev. Corp.

Baysal, E. (1982). Modeling and migration by the Fourier transform method(Doctoral dissertation, University of Houston Central Campus).

Baysal, E., Kosloff, D. D., & Sherwood, J. W. (1983). Reverse time migration.Geophysics, 48(11), 1514-1524.

Bohlen, T. (2002). Parallel 3-D viscoelastic finite difference seismic modelling. Computers & Geosciences, 28(8), 887-899.

Cerjan, C., Kosloff, D., Kosloff, R., & Reshef, M. (1985). A nonreflecting boundary condition for discrete acoustic and elastic wave equations.Geophysics, 50(4), 705-708.

Chang, W. F., & McMechan, G. A. (1986). Reverse-time migration of offset vertical seismic profiling data using the excitation-time imaging condition. Geophysics, 51(1), 67-84.

Chang, W. F., & McMechan, G. A. (1987). Elastic reverse-time migration.Geophysics, 52(10), 1365-1375.

Chattopadhyay, S., & McMechan, G. A. (2008). Imaging conditions for prestack reverse-time migration. Geophysics, 73(3), S81-S89.

Chen, K. H. (1987, October). Reverse-time profile migration. In 1987 SEG Annual Meeting.

Chen, H. W., & McMechan, G. A. (1992). 3-D pre-stack depth migration for salt and subsalt structures using reverse-VSP data. Journal of Seismic Exploration,1(3), 281-291.

Claerbout, J. F. (1971). Toward a unified theory of reflector mapping.Geophysics, 36(3), 467-481.

Claerbout, J. F. (1985). Imaging the earth's interior (Vol. 316). Oxford: Blackwell scientific

publications.

Courant, R., & Hilbert, D. Methods of Mathematical Physics (Interscience, New York, 1962). Vol. II, 32-39.

Greenberg, M. L., & Castagna, J. P. (1992). SHEARWAVE VELOCITY ESTIMATION IN POROUS ROCKS: THEORETICAL FORMULATION, PRELIMINARY VERIFICATION AND APPLICATIONS1. Geophysical prospecting, 40(2), 195-209.

CREWES Zoeppritz Explorer. (2014, June 18). . Retrieved , from http://www.crewes.org/ResearchLinks/ExplorerPrograms/ZE/ZEcrewes.html

Gyrfi, Istvn, Zoltan Hajnal, Don J. White, and B. Roberts. "High-resolution 2D and 3D seismic imaging of structurally complex hardrock environments hosting high-grade uranium ore, Athabasca Basin, Canada." In 2004 SEG Annual Meeting. Society of Exploration Geophysicists, 2004.

Gyorfi, I., Z. Hajnal, D. J. White, E. Takacs, B. Reilkoff, I. R. Annesley, B. Powell, and R. Koch. "High-resolution seismic survey from the McArthur River region: Contributions to mapping of the complex P2 uranium ore zone, Athabasca Basin, Saskatchewan." BULLETIN-GEOLOGICAL SURVEY OF CANADA 588 (2007): 397.

Hajnal, Z., B. Pandit, B. Reilkoff, E. Takacs, I. Annesley, and D. Wallster. "Recent development in 2D and 3D seismic imaging of high-grade uranium ore deposit related environments, in the Eastern Athabasca Basin, Canada." InExploration in the new millennium: Proceedings of the Fifth Decennial International Conference on Mineral Exploration, edited by B. Milkereit, pp. 1131-1135. 2007.

Hajnal, Z., D. J. White, E. Takacs, I. Gyorfi, I. R. Annesley, G. Wood, C. ODowd, and G. Nimeck. "Application of modern 2-D and 3-D seismic-reflection techniques for uranium exploration in the Athabasca Basin." Canadian Journal of Earth Sciences 47, no. 5 (2010): 761-782.

Hecht, L., and M. Cuney. "Hydrothermal alteration of monazite in the Precambrian crystalline basement of the Athabasca Basin (Saskatchewan, Canada): implications for the formation of unconformity-related uranium deposits." Mineralium Deposita 35, no. 8 (2000): 791-795.

Hilterman, F. J. (1989, January). Is AVO the seismic signature of rock properties?. In 1989 SEG Annual Meeting. Society of Exploration Geophysicists.

Hilterman, F. J. (2001). Seismic amplitude interpretation: 2001 distinguished instructor short course (No. 4). SEG Books.

Hoeve, J., and T. I. I. Sibbald. "Uranium metallogenesis and its significance to exploration in the Athabasca Basin." (1978): 161-188.

Hokstad, K., Mittet, R., & Landr, M. (1998). Elastic reverse time migration of marine walkaway vertical seismic profiling data. Geophysics, 63(5), 1685-1695.

Holberg, O. (1987). Computational aspects of the choice of operator and sampling interval for numerical differentiation in large-scale simulation of wave phenomena. Geophysical prospecting, 35(6), 629-655.

Houser, C., Masters, G., Shearer, P., & Laske, G. (2008). Shear and compressional velocity models of the mantle from cluster analysis of longperiod waveforms. Geophysical Journal International, 174(1), 195-212.

Jefferson, C. W., D. J. Thomas, S. S. Gandhi, P. Ramaekers, G. Delaney, D. Brisbin, C. Cutts, P. Portella, and R. A. Olson. "Unconformity-associated uranium deposits of the Athabasca Basin, Saskatchewan and Alberta."BULLETIN-GEOLOGICAL SURVEY OF CANADA 588 (2007): 23.

Juhojuntti, Niklas, Garnet Wood, Christopher Juhlin, Clare ODowd, Peter Dueck, and Calin Cosma. "3D seismic survey at the Millennium uranium deposit, Saskatchewan, Canada: Mapping depth to basement and imaging post-Athabasca structure near the orebody." Geophysics 77, no. 5 (2012): WC245-WC258.

Keho, T. H. (1984, December). Kirchhoff migration for vertical seismic profiles. In 1984 SEG Annual Meeting.

Kelly, K. R., Ward, R. W., Treitel, S., & Alford, R. M. (1976). Synthetic seismograms: a finite-difference approach. Geophysics, 41(1), 2-27.

Khler, K., & Koenig, M. (1986). Reconstruction of reflecting structures from vertical seismic profiles with a moving source. Geophysics, 51(10), 1923-1938.

Kosloff, D. D., & Baysal, E. (1982). Forward modeling by a Fourier method.Geophysics, 47(10), 1402-1412.

Levin, S. A. (1984). Principle of reverse-time migration. Geophysics, 49(5), 581-583.

LiU, HsiPing, Don L. Anderson, and Hiroo Kanamori. "Velocity dispersion due to anelasticity; implications for seismology and mantle composition."Geophysical Journal of the Royal Astronomical Society 47, no. 1 (1976): 41-58.

Mavko, G., Mukerji, T., & Dvorkin, J. (2009). The rock physics handbook: Tools for seismic analysis of porous media. Cambridge University Press.

McMechan, G. A. (1982). Determination of source parameters by wavefield extrapolation.

Geophysical Journal International, 71(3), 613-628.

McMECHAN, G. A. "Migration by extrapolation of time-dependent boundary values." Geophysical Prospecting 31.3 (1983): 413-420.

Mwenifumbo, C. J., Elliott, B. E., Jefferson, C. W., Bernius, G. R., & Pflug, K. A. (2004). Physical rock properties from the Athabasca Group: designing geophysical exploration models for unconformity uranium deposits. Journal of applied geophysics, 55(1), 117-135.

Mwenifumbo C. J.; Percival J. B.; Bernius G. R.; Elliott B.; Jefferson C. W.; Wasyliuk K.; Drever G. Comparison of geophysical, mineralogical, and stratigraphic attributes in drillholes MAC-218 and RL-88, McArthur River uranium camp, Athabasca Basin, Saskatchewan. Bulletin - Geological Survey of Canada 4(18) (2007): 507-520

Nur, A., Marion, D., & Yin, H. (1991). Wave velocities in sediments. In Shear waves in marine sediments (pp. 131-140). Springer Netherlands.

Olver, P. J. (2013). Numerical method. (pp. 151-182). DOI: dpo.cusat.ac.in/msc/oce2302/notes/numerical methods/nfd.pdf

Ramaekers, P., C. W. Jefferson, G. M. Yeo, B. Collier, D. G. F. Long, G. Drever, S. McHardy, D. Jiricka, C. Cutts, and K. Wheatley. "Revised geological map and stratigraphy of the Athabasca Group, Saskatchewan and Alberta."BULLETIN-GEOLOGICAL SURVEY OF CANADA 588 (2007): 155.

Reuss, A., & Angnew, Z. (1929). A calculation of the bulk modulus of polycrystalline materials. Math Meth, 9, 55.

Rietbrock, A., & Scherbaum, F. (1994). Acoustic imaging of earthquake sources from the Chalfant Valley, 1986, aftershock series. Geophysical Journal International, 119(1), 260-268.

Schreiner, B. T. "Quaternary Geology of the NEA/IAEA Athabasca Test Area."Uranium Exploration in the Athabasca Basin; GSC Paper (1983): 82-11.

Sun, R. O. B. E. R. T., & McMECHAN, G. A. (1986). Pre-stack reverse-time migration for elastic waves with application to synthetic offset vertical seismic profiles. Proceedings of the IEEE, 74(3), 457-465.

Sun, Langqiu F., Bernd Milkereit, and Douglas R. Schmitt. "Measuring velocity dispersion and attenuation in the exploration seismic frequency band."Geophysics 74, no. 2 (2009): WA113-WA122.

Sun, Langqiu F. "velocity dispersion of seismic wave in the near-surface and its effect on seis-

mic imaging for hardrock." Tectonophysics. (2013)

Wang, Z., & Nur, A. (1992). Elastic wave velocities in porous media: a theoretical recipe. Seismic and acoustic velocities in reservoir rocks, 2, 1-35.

White, D. J., Z. Hajnal, B. Roberts, I. Gyorfi, B. Reilkoff, G. Bellefleur, C. Mueller, S. Woelz, C. J. Mwenifumbo, and E. Takacs. "Seismic methods for uranium exploration: an overview of EXTECH IV seismic studies at the McArthur River mining camp, Athabasca Basin, Saskatchewan." BULLETIN-GEOLOGICAL SURVEY OF CANADA 588 (2007): 363.

Wiggins, J. W. (1984). Kirchhoff integral extrapolation and migration of nonplanar data. Geophysics, 49(8), 1239-1248.

Yilmaz, . (2001). Seismic data analysis: processing, inversion, and interpretation of seismic data (No. 10). SEG Books.